

Reduced platelet forces underlie impaired hemostasis in mouse models of *MYH9*-related disease

Juliane Baumann^{1†}, Laura Sachs^{2†}, Oliver Otto^{3,4}, Ingmar Schoen⁵, Peter Nestler³, Carlo Zaninetti^{2,6}, Martin Kenny⁵, Ruth Kranz¹, Hendrik von Eysmondt⁷, Johanna Rodriguez⁷, Tilman E. Schäffer⁷, Zoltan Nagy¹, Andreas Greinacher², Raghavendra Palankar^{2*}, Markus Bender^{1*†}

***MYH9*-related disease patients with mutations in the contractile protein nonmuscle myosin heavy chain IIA display, among others, macrothrombocytopenia and a mild-to-moderate bleeding tendency. In this study, we used three mouse lines, each with one point mutation in the *Myh9* gene at positions 702, 1424, or 1841, to investigate mechanisms underlying the increased bleeding risk. Agonist-induced activation of *Myh9* mutant platelets was comparable to controls. However, myosin light chain phosphorylation after activation was reduced in mutant platelets, which displayed altered biophysical characteristics and generated lower adhesion, interaction, and traction forces. Treatment with tranexamic acid restored clot retraction in the presence of tPA and reduced bleeding. We verified our findings from the mutant mice with platelets from patients with the respective mutation. These data suggest that reduced platelet forces lead to an increased bleeding tendency in patients with *MYH9*-related disease, and treatment with tranexamic acid can improve the hemostatic function.**

Copyright © 2022
The Authors, some
rights reserved;
exclusive licensee
American Association
for the Advancement
of Science. No claim to
original U.S. Government
Works. Distributed
under a Creative
Commons Attribution
NonCommercial
License 4.0 (CC BY-NC).

INTRODUCTION

The platelet cytoskeleton ensures normal size and the discoid shape under resting conditions and undergoes rapid rearrangement upon activation. Platelets respond to the biophysical properties of the extracellular environment through integrin-based adhesion sites, which results in actomyosin-mediated contractile forces (1, 2). Several inherited platelet bleeding disorders are caused by mutations in key cytoskeletal-regulatory proteins (3). *MYH9*-related disease (*MYH9*-RD) is a rare inherited platelet disorder (4). The *MYH9* gene encodes the heavy chain of nonmuscle myosin IIA, an actin-binding protein with contractile properties. Heterozygous mutations in the *MYH9* gene in humans lead to macrothrombocytopenia with a moderate bleeding tendency. Depending on the position of the mutations [>>30 mutations identified (5)], the risk increases for other syndromic manifestations such as renal failure, hearing loss, and presenile cataract (5–7). Patients with a mutation at amino acid position 702, located in the motor domain of nonmuscle myosin IIA, are reported to be most affected for nonhematologic defects and have a higher risk for increased bleeding. Mutations located in the rod domain (amino acid positions 1424 and 1841) cause a milder phenotype (5). Three different mouse lines with the knock-in mutations Arg702Cys (R702C), Asp1424Asn (D1424N), and Glu1841Lys (E1841K) were generated (8), which are the most frequent mutations found in human patients (9). These heterozygous point-mutated mice recapitulated key features of human patients, such as

macrothrombocytopenia, moderately prolonged bleeding times, decreased ability to retract clots, and nonhematologic defects (8). These data show that myosin IIA plays a vital role in platelet production and plug stabilization. However, it is insufficiently understood which factors contribute to the hemostatic defect observed in patients with *MYH9*-RD and mutant mice. Given the central role of myosin IIA in force generation and the increased bleeding risk in patients with *MYH9*-RD, a better understanding of the underlying biophysical mechanisms in clot formation and its stabilization is warranted (10).

Recently, it was demonstrated that biophysical signatures are similar between human and murine platelets (11). Therefore, we took advantage of the heterozygous R702C, D1424N, and E1841K point-mutated *Myh9* mice and comprehensively investigated whether altered biomechanical properties might be responsible for the increased bleeding phenotype. While the primary function of mutant mouse platelets was comparable to controls, phosphorylation of the myosin light chain after activation was strongly reduced, the extent of clot retraction was decreased, and thrombi were more unstable even when platelet count was adjusted. In line with this, biophysical analyses revealed that *Myh9* mutant platelets generate lower adhesion forces to collagen, lower interaction forces between platelets, and reduced traction forces when spread on fibrinogen-coated micropost arrays. We verified our key findings by analyzing the biophysical function of platelets isolated from patients with *MYH9*-RD having the respective mutation. Last, we observed that treatment with the antifibrinolytic agent, tranexamic acid (TXA), restored clot retraction and reduced bleeding in all three mouse lines. These data suggest that the most common *MYH9*-RD mutations impair the generation of contractile forces by myosin IIA that is necessary to prevent increased bleeding.

RESULTS

Unaltered activation but impaired deformability of *Myh9* mutant platelets

While the role of platelets in hemostatic plug and thrombus formation has been intensively studied from a biological perspective, the

¹Institute of Experimental Biomedicine—Chair I, University Hospital and Rudolf Virchow Center, Würzburg, Germany. ²Institute for Immunology and Transfusion Medicine, University Medicine Greifswald, Greifswald, Germany. ³Zentrum für Innovationskompetenz—Humorale Immunreaktionen bei Kardiovaskulären Erkrankungen, University Greifswald, Greifswald, Germany. ⁴Deutsches Zentrum für Herz-Kreislauf-Forschung e. V., Standort Greifswald, Universitätsmedizin Greifswald, Greifswald, Germany. ⁵School of Pharmacy and Biomolecular Sciences, Irish Centre for Vascular Biology, Royal College of Surgeons in Ireland, Dublin, Ireland. ⁶University of Pavia, Pavia, Italy. ⁷Institute of Applied Physics, University of Tübingen, Tübingen, Germany.

*Corresponding author. Email: bender_m1@ukw.de (M.B.); palankarr@uni-greifswald.de (R.P.)

†These authors contributed equally to this work.

mechanobiological aspects are only poorly understood. To investigate the biological and biophysical properties of the contractile protein nonmuscle myosin IIA, we capitalized on mice with three different point mutations in the *Myh9* gene. Most results of the D1424N mutation are shown in the main manuscript; results regarding the R702C and E1841K mutations are shown in the Supplementary Materials. We confirmed the presence of the protein myosin IIA in platelet lysates from control and heterozygous mutant mice (*Myh9*^{R702C/+}, *Myh9*^{D1424N/+}, and *Myh9*^{E1841K/+}) by Western blot analysis (fig. S1, A and B). The expression levels of nonmuscle myosin IIA were comparable to controls (fig. S1C). *Myh9* mutant mice displayed a significant reduction in platelet count and increased platelet size as determined by a hematology analyzer (Fig. 1, A and B, and fig. S2, A and B) (8). Other blood parameters such as red blood cell count, hematocrit, and hemoglobin were unaltered in mutant mice (table S1). Because of the increased platelet size in mutant mice, control and mutant platelets were gated for a population of similar size in glycoprotein expression and platelet activation studies (fig. S2C). Analysis of expression of prominent platelet surface proteins by flow cytometry revealed moderate differences of some receptors, most notably the glycoprotein (GP) Ib-V-IX complex, even when comparing platelet populations of similar size (Fig. 1C and fig. S2, C and D). Next, surface exposure of P-selectin and activation of the platelet integrin αIIbβ3 was analyzed after incubation with different agonists. Overall comparable results were obtained for control and mutant platelets after stimulation of heterotrimeric GTP-binding protein-coupled receptors with adenosine diphosphate (ADP), the thromboxane A2 analog U46619, a combination of both, or thrombin (Fig. 1, D and E, and fig. S3, A and B). Similarly, *Myh9* mutant platelets exhibited a comparable degree of activation upon stimulation of the GPVI-ITAM (immunoreceptor tyrosine-based activation motif) pathway with collagen-related peptide (CRP) or convulxin and of the hemITAM receptor, CLEC2 (C-type lectin-like receptor 2), with rhodocytin. To clarify the role of mutated myosin IIA for platelet shape change and aggregation, in vitro aggregation studies were performed. Both agonists, Horm collagen and thrombin, induced a comparable activation-dependent shape change of control and mutant platelets (fig. S4, A and B). Furthermore, *Myh9* mutant platelets showed a normal onset and degree of aggregation (fig. S4, A and B, and table S2). Next, we investigated whether the mutation in myosin IIA leads to ultrastructural changes in platelets. Transmission electron microscopic (TEM) analysis of mutant platelets revealed a heterogeneous population of platelet size but an otherwise comparable ultrastructure (Fig. 1F and fig. S4C). Together, *Myh9* point-mutated mice display a macrothrombocytopenia, and their platelets can get activated and form aggregates in response to platelet agonists.

In contrast, real-time fluorescence deformability cytometry (RT-FDC) measurements revealed a significantly decreased deformation and increased size of *Myh9* mutant platelets (Fig. 1G and fig. S5, A and B), which points to an increased Young's modulus. Since most agonist-induced platelet functions were otherwise normal, we further investigated the structure and function of cytoskeletal components.

Decreased phosphorylation of the myosin light chain in *Myh9* mutant platelets

To test possible differences in F-actin content, we performed flow cytometry with phalloidin-stabilized resting platelets. Mutant platelets exhibited an increased F-actin content, most likely because of the increased platelet size (Fig. 2A and fig. S6A). To investigate the

organization and rearrangement of the cytoskeleton in *Myh9* mutant platelets, we performed spreading experiments on a fibrinogen-coated surface. Differential interference contrast imaging revealed comparable spreading kinetics of *Myh9*^{R702C/+} mutant platelets and slightly faster spreading of *Myh9*^{D1424N/+} and *Myh9*^{E1841K/+} mutant platelets on a fibrinogen-coated surface (Fig. 2B and fig. S6B). The increased size might explain the faster adhesion kinetics of these platelets. Similar to control platelets, mutant platelets were able to rearrange the cytoskeleton and form filopodia and lamellipodia, as revealed by platinum replica electron and confocal microscopy (Fig. 2C and fig. S6, C and D). Phosphorylation of the myosin light chain 2 (MLC2) is responsible for the generation of contractile forces in platelets. Therefore, a capillary-based immunoassay approach was used to detect MLC2 phosphorylation in resting and thrombin-activated platelets. MLC2 and myosin phosphatase 1 (MYPT1) expression were comparable in control and mutant samples (Fig. 2D and figs. S1B and 7A). However, phosphorylation of MLC2 after activation with thrombin was strongly reduced to 56% in *Myh9*^{D1424N/+}, to 40% in *Myh9*^{R702C/+}, and to 58% *Myh9*^{E1841K/+} mutant platelets compared to *Myh9*^{+/+} controls (Fig. 2D and fig. S7, A and B). Although we have not identified the interaction of myosin heavy and light chain of mutant myosin IIA, we can hypothesize no impaired interaction. The instability of the regulatory light chain upon the absence or interrupted interaction of the heavy chain would result in rapid degradation of MLC (12–14). In contrast, we observed no alteration in MLC2 total expression. These data suggest that heterozygous mutations in the motor domain (R702C) and rod domain (D1424N and E1841K) might impair the mutant platelets' contractile properties.

Low contractile force generation and impaired clot retraction of *Myh9* mutant platelets

To measure contractile forces, platelets were allowed to adhere and spread on fibrinogen-coated micropost arrays and pulled at posts to different extents. The mean traction force per post beneath each cell was significantly reduced by 38% in *Myh9*^{D1424N/+}, 29% in *Myh9*^{R702C/+}, and 28% in *Myh9*^{E1841K/+} platelets compared to their corresponding controls, as readily perceived from the images of the deformed posts [Fig. 3A (arrows) and fig. S8]. However, the total force per cell was not significantly different for *Myh9*^{D1424N/+} platelets because of the larger platelet volume of mutant platelets (Fig. 1B), which compensated for the lower reduced intrinsic contractility (Fig. 3A). The total traction forces per single platelet in *Myh9*^{R702C/+} and *Myh9*^{E1841K/+} compared to control platelets were significantly lower, indicating that their platelet volume, which is not as increased as for *Myh9*^{D1424N/+} platelets (Fig. 1B and fig. S2B), was not sufficient to compensate for the reduced intrinsic contractility (fig. S8). Platelets spread on a fibrinogen-coated surface were also analyzed for stiffness using scanning ion conductance microscopy (SICM). *Myh9*^{R702C/+} and *Myh9*^{D1424N/+} platelets displayed a softer appearance on fibrinogen compared to *Myh9*^{+/+} platelets, as revealed by a lower Young's modulus (Fig. 3B and fig. S9). In contrast, *Myh9*^{E1841K/+} platelets showed a comparable Young's modulus to *Myh9*^{+/+} platelets (fig. S9). Next, we performed a clot retraction assay since platelet-mediated compaction is an important mechanism to stabilize thrombi (10). The extent of clot retraction was significantly different between control and mutant mice. *Myh9* mutant samples showed an impaired clot retraction (8), even when the platelet count had been adjusted to 3×10^5 platelets/ μl (Fig. 3C and fig. S10, A and C). Quantification of the residual clot revealed a

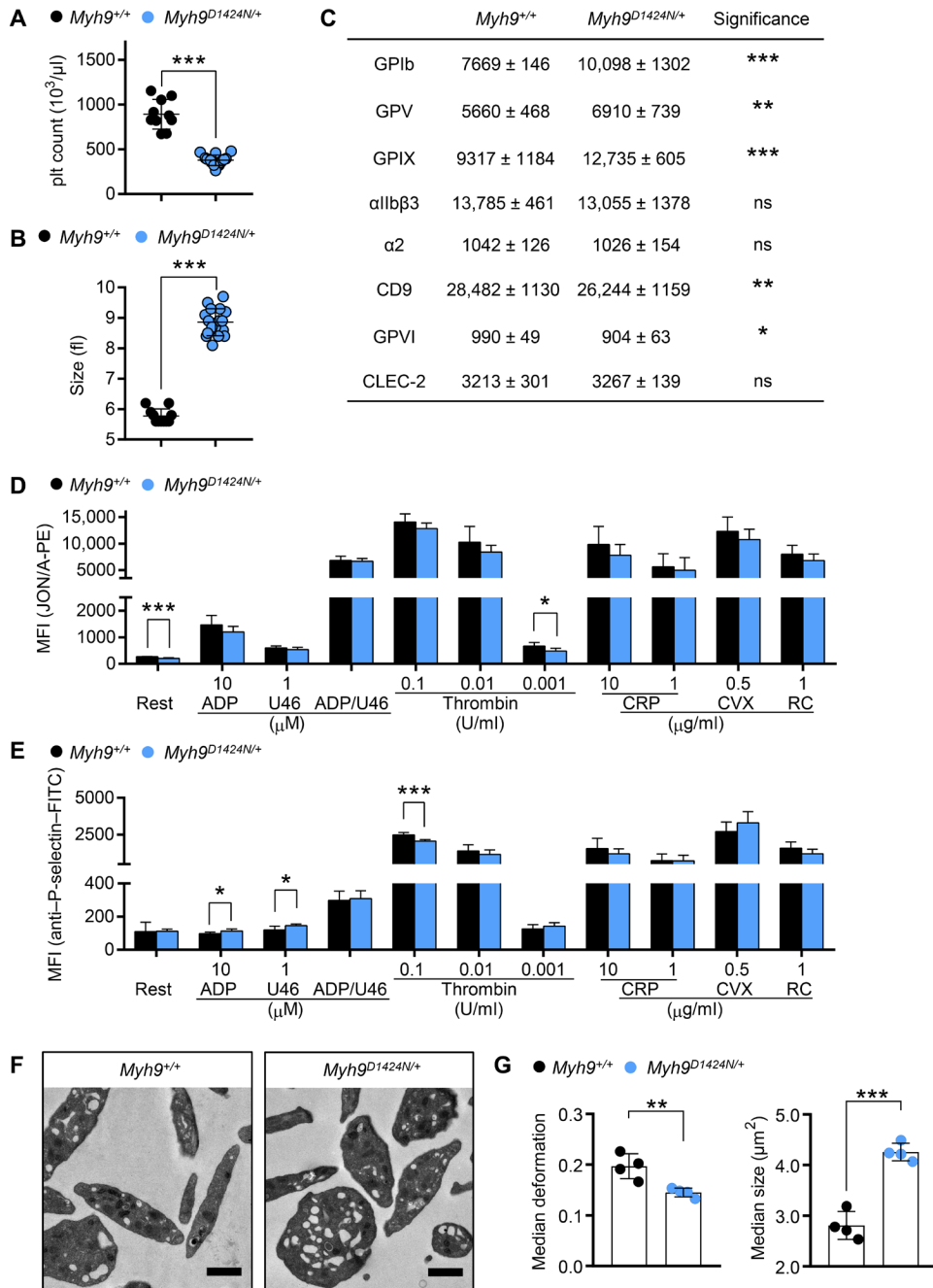


Fig. 1. Mutation in *Myh9* gene impairs platelet size and stiffness. (A) Platelet count per microliter and (B) platelet size of $\text{Myh9}^{+/+}$ and $\text{Myh9}^{\text{D1424N}+/}$ mice were determined by a hematology analyzer. (A and B) Each symbol represents one individual mouse (mean ± SD; Mann-Whitney *U* test, *** $P < 0.001$). (C) Expression of glycoproteins on the platelet surface was determined by flow cytometry ($n = 6$). (D) Activation of platelet $\alpha\text{IIb}\beta3$ -integrin [JON/A-phycoerythrin (PE)] and (E) α -granule release [anti-P-selectin-fluorescein isothiocyanate (FITC)] were assessed under resting (Rest) conditions and upon stimulation with different agonists by flow cytometry ($n = 6$). U46: thromboxane A2 analog U46619; CVX: convulxin; RC: rhodocytin. (C to E) Data are expressed as mean fluorescence intensity (MFI). (F) Transmission electron micrographs from $\text{Myh9}^{+/+}$ and $\text{Myh9}^{\text{D1424N}+/}$ platelets; scale bars, 1 μm . (G) Each data point of RT-FDC measurement shows the median deformation or median area of at least 2000 platelets from one subject, and bar plots show means ± SD of platelet deformation or platelet area ($n = 4$). Statistics: multiple comparison using Holm-Sidak [not significant (ns), $P \geq 0.05$; * $0.05 > P \geq 0.01$, ** $0.01 > P \geq 0.001$; and *** $P < 0.001$].

heavier, less retracted clot and a corresponding lower volume of residual fluid in *Myh9* mutant samples (Fig. 3D and fig. S10, B and D). These findings strongly suggest that impaired clot retraction of *Myh9* mutant platelets is due to a defect in the generation of contractile forces and not because of a reduction in platelet count.

Lower adhesion and interaction forces of mutant platelets

To investigate the mechanisms of platelet biomechanics under shear flow, we analyzed the effect of the heterozygous point mutations in myosin IIA in an ex vivo thrombus formation assay. At first, we studied platelet adhesion to collagen fibers in a whole-blood

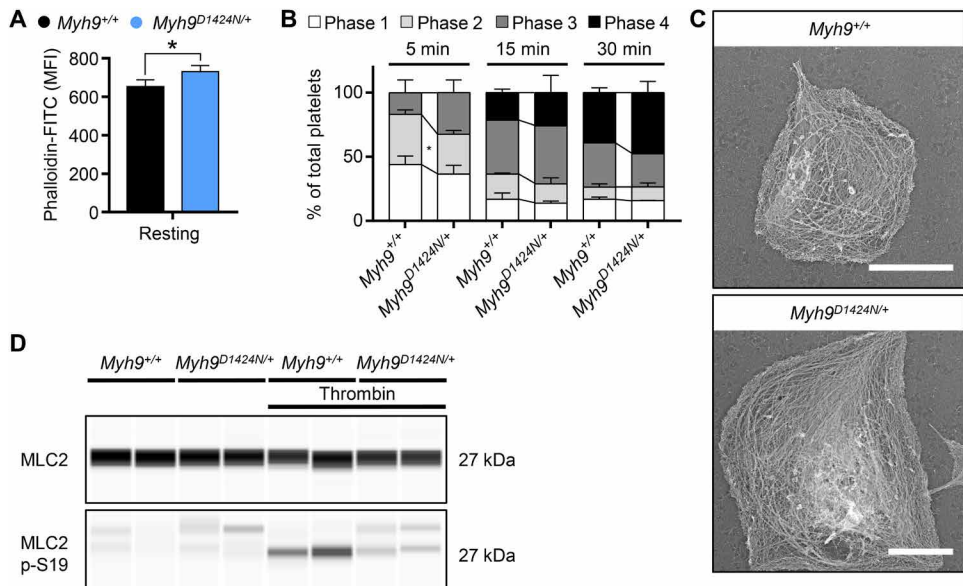


Fig. 2. Phosphorylation of MLC2 is decreased in *Myh9^{D1424N/+}* platelets. (A) F-actin content of resting platelets was measured by flow cytometry after incubation with phalloidin-FITC ($n = 3$ to 7). The MFI is shown. (B) Statistical analysis of the different spreading phases (phase 1, resting platelets; phase 2, platelets forming filopodia; phase 3, platelets forming lamellipodia and filopodia; and phase 4, fully spread platelets) of fixed *Myh9^{+/+}* and *Myh9^{D1424N/+}* platelets on fibrinogen at different time points expressed as mean \pm SD ($n = 2$). (C) Representative PREM (platinum replica electron microscopy) images of the cytoskeleton ultrastructure of platelets spread on fibrinogen in the presence of thrombin (scale bars, 2 μ m). (D) Expression of MLC2 and phosphorylated MLC2p-S19 in resting and thrombin-activated (0.05 U/ml, 1 min) platelets was determined by using an automated quantitative capillary-based immunoassay platform, Jess (ProteinSimple). Representative immunoblot of three independent experiments is shown ($n = 2$). Statistics: multiple comparison using Holm-Sidak (* $0.05 > P \geq 0.01$).

perfusion assay at shear rates of 1000 s $^{-1}$. Control and mutant platelets adhered to collagen and formed thrombi both under platelet count adjusted (5×10^5 platelets/ μ l) and unadjusted conditions. However, platelets from *Myh9^{D1424N/+}* and *Myh9^{R702C/+}* mutant mice formed fewer and smaller thrombi than controls (Fig. 4A and fig. S11A). Unexpectedly, platelets from *Myh9^{E1841K/+}* mutant mice formed only fewer and smaller thrombi under thrombocytopenic conditions (fig. S11A). Next, platelet adhesion forces on collagen were measured using single-platelet force spectroscopy (SPFS). Platelets of *Myh9* mutant mice displayed lower adhesion forces to collagen (reduced by 69% in *Myh9^{D1424N/+}*, by 33% in *Myh9^{R702C/+}*, and by 42% in *Myh9^{E1841K/+}* platelets; Fig. 4B and fig. S11B). Similarly, interaction forces between two single platelets were reduced for all three mouse lines (*Myh9^{D1424N/+}* by 39%, *Myh9^{R702C/+}* by 50%, and *Myh9^{E1841K/+}* by 29%; Fig. 4C and fig. S11C). Thrombi formed at a shear rate of 1000 s $^{-1}$ on collagen were analyzed for their stiffness by colloidal probe spectroscopy. Thrombi formed by platelets of *Myh9* mutant mice were softer compared to thrombi of control mice, as revealed by a decreased Young's modulus (Fig. 4D and fig. S11D). In summary, these results suggest that reduced platelet-substrate and platelet-platelet forces lead to reduced thrombus formation under shear.

Samples of patients with MYH9-RD recapitulate the biomechanical phenotype observed in the respective mutant mice

To verify our biophysical results obtained from the analyses of mutant mice, we analyzed deformability and force generation of platelets from two patients with the respective mutations (*MYH9* p.D1424N and *MYH9* p.E1841K). Mechanophenotyping using RT-FDC

showed that platelets from patients are less deformable and larger, which is in line with the mouse data (Fig. 5A and fig. S12A). Other blood parameters such as red blood cell count, hematocrit, and hemoglobin were unaltered in patient blood (table S3). Next, we assessed platelet adhesion and thrombus formation on collagen under shear. We observed significantly less and smaller thrombi when whole patient blood was perfused over collagen fibers. Moreover, the kinetics of thrombus formation overtime was decreased in the patient sample (Fig. 5B and fig. S12B). We measured the stiffness of the formed thrombi by colloidal probe spectroscopy. In agreement with the data obtained from *Myh9^{D1424N/+}* mutant mice, thrombi were significantly softer for *MYH9* p.D1424N (Fig. 5C). In contrast, stiffness was moderately but not significantly reduced for *MYH9* p.E1841K (fig. S12C). These results show that the mechanical characteristics of human and mouse platelets with point mutations in nonmuscle myosin IIA are overall comparable, except for thrombus stiffness of the *MYH9* p.E1841K sample, which shows only a tendency to softer thrombi.

Treatment with TXA improves hemostatic function in mutant mice

Patients with *MYH9*-RD have an increased bleeding risk. The anti-fibrinolytic drug, TXA, is one option to control bleeding complications in those patients (5, 6). We thus hypothesized that gaps of a less compact clot might allow for increased diffusion of plasminogen into the clot, thereby accelerating clot instability and that TXA may help prevent clot degradation and stabilize the clot of *Myh9* mutant mice. TXA was beneficial in combination with threshold concentration (0.0138 nM; fig. S13A) of the recombinant tissue plasminogen activator (rtPA) (Fig. 6A). The addition of clinically

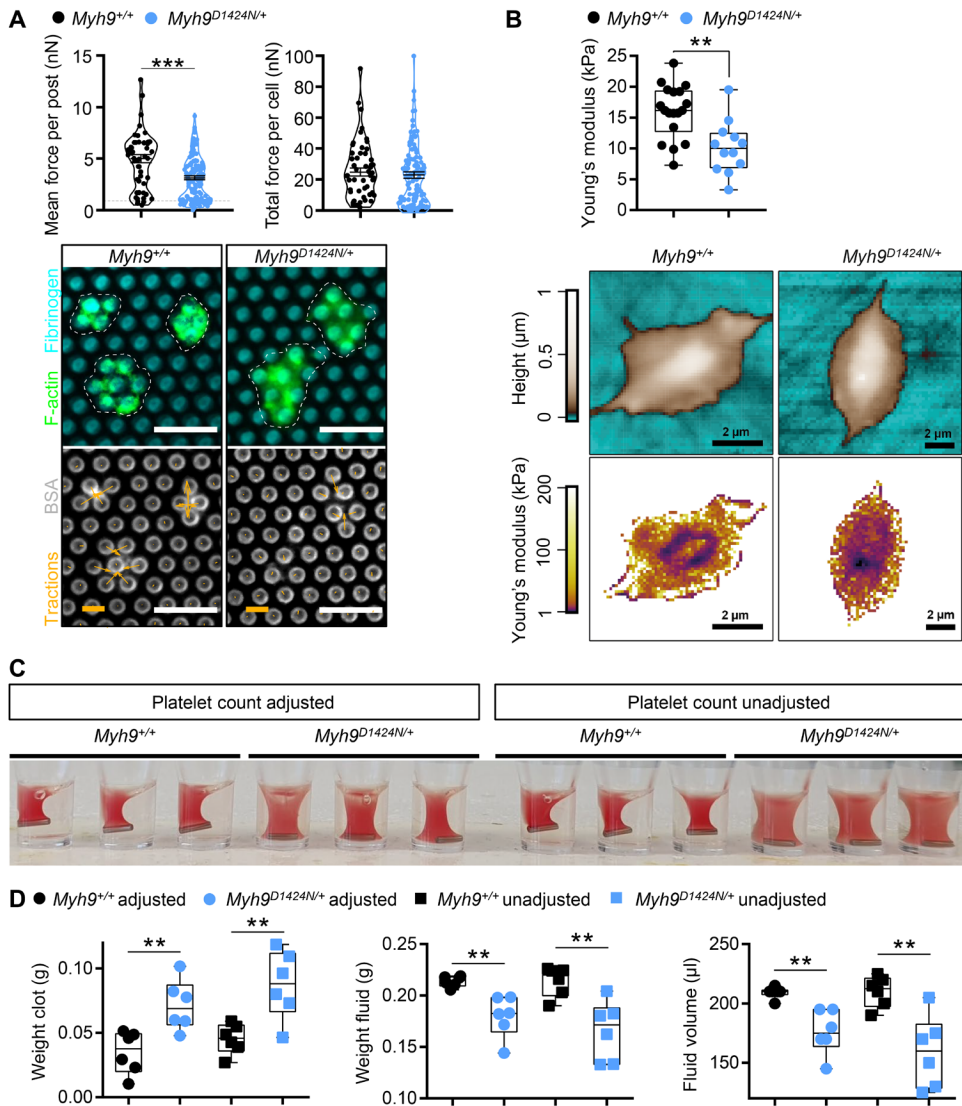


Fig. 3. Less contractile forces and reduced clot retraction of Myh9 mutant platelets. (A) Platelet contractile forces were measured per post and the sum of posts per cell (mean \pm SD; Myh9^{+/+}: n = 51 platelets; Myh9^{D1424N/+}: n = 124 platelets). Representative images of individual platelets (dashed white line), stained for F-actin, and its traction on microposts stained for fibrinogen, and bovine serum albumin (BSA; scale bars, 5 μ m, force bar, 10 nN). Statistics: Mann-Whitney U test (ns, P \geq 0.05; ***P < 0.001). (B) Washed Myh9^{+/+} and Myh9^{D1424N/+} platelets spread on fibrinogen in the presence of thrombin (as well as their Young's modulus) were analyzed using SICM. Each symbol represents one platelet (Myh9^{+/+}: n = 20 platelets; Myh9^{D1424N/+}: n = 12 platelets), and box plots represent median \pm SD (statistics: Mann-Whitney U test, **0.01 > P \geq 0.001). Representative images showing the height (upper row) or Young's modulus (lower row) of Myh9^{+/+} and Myh9^{D1424N/+} platelets. (C) Representative image of clot formation at time point 60 min (n = 3). (D) Statistical analysis of weight from residual clot and fluid and of volume from residual fluid depicts median \pm SD. Each symbol represents one individual mouse (multiple comparison using Holm-Sidak, **0.01 > P \geq 0.001).

relevant TXA concentration of 100 μ M inhibited the fibrinolytic effect of rtPA and restored clot retraction under platelet count unadjusted conditions (Fig. 6, A and B, and fig. S13B and S14). However, TXA in a concentration of 1 μ M was too low to restore clot retraction. No adverse effects could be observed at high concentrations of 10 mM TXA. As expected (8), Myh9 mutant mice displayed prolonged bleeding times (Fig. 6C and fig. S15). TXA concentration of 10 μ g/g was injected to induce a plasma concentration measured in humans of 15 mg/liter resulting in substantial inhibition of fibrinolysis (15). Notably, treatment with TXA substantially reduced the bleeding time in the three Myh9 mutant mouse models (Fig. 6C and

fig. S15). In summary, the increased bleeding phenotype due to reduced platelet forces in Myh9 mutant mice can be compensated by the addition of TXA.

TXA delays clot lysis of samples from patients with MYH9-RD

The improved clot stability of mutant mouse samples prompted us to test the effect of TXA on clot formation and stability in patient samples. While the onset of lysis (LOT) measured by thromboelastometry occurred earlier for the human patient sample when adding rtPA, the addition of TXA rescued the defect (Fig. 7A and fig. S16). Similarly, ex vivo thrombus stability of MYH9-RD patient

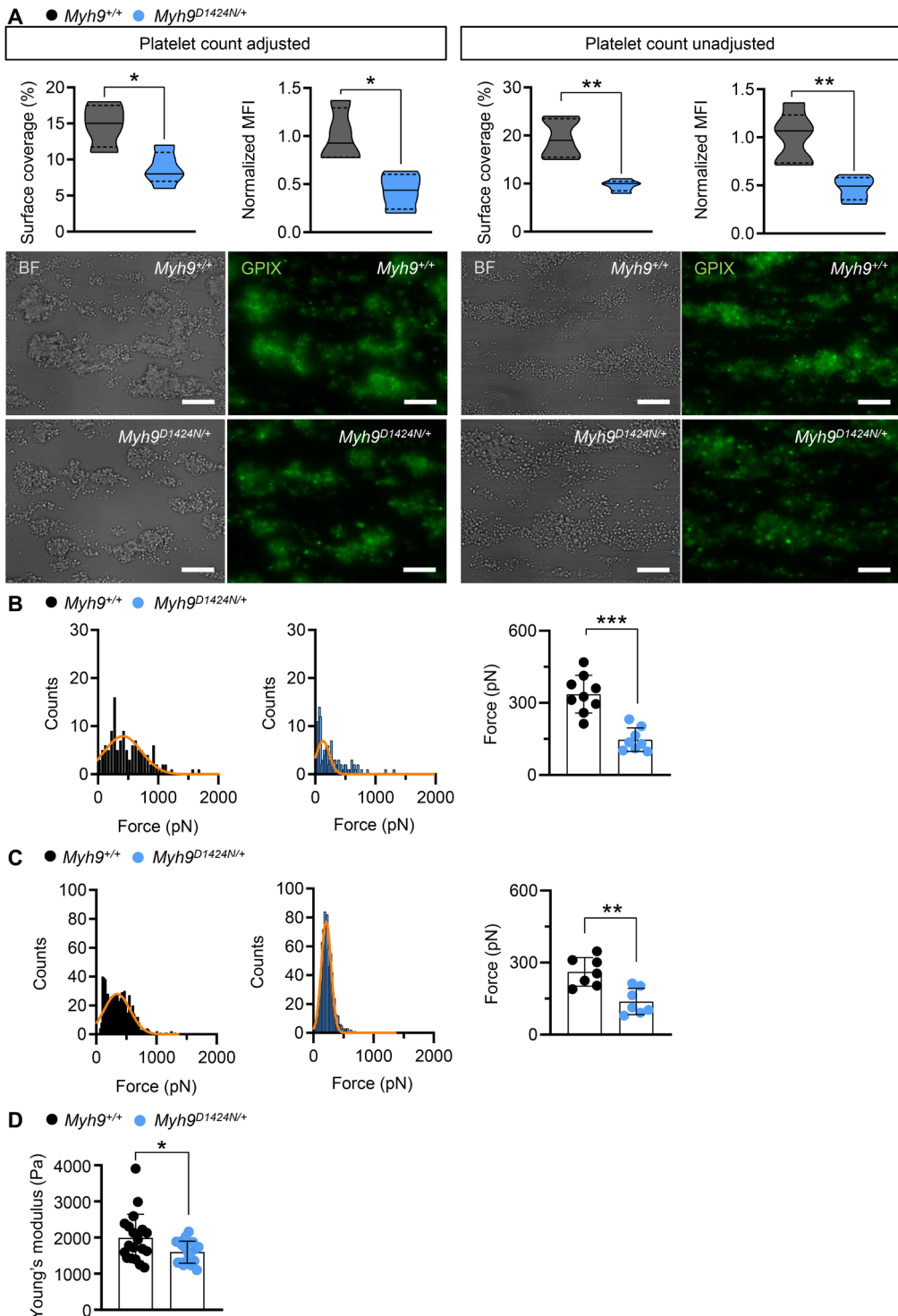


Fig. 4. Lower adhesion and interaction forces of $Myh9^{D1424N/+}$ platelets lead to smaller and softer thrombi. (A) Assessment of platelet adhesion and aggregate formation under flow (1000 s^{-1}) on collagen of $Myh9^{+/+}$ and $Myh9^{D1424N/+}$ samples. Analysis of the surface area covered by platelets (%) and the relative normalized thrombus MFI of anti-GPIX (Alexa Fluor 488) are shown under platelet count adjusted conditions on the left side (mean \pm SD; $n = 4$) and unadjusted conditions on the right side (mean \pm SD; $n = 5$). Respective representative images taken at the end of the perfusion time are shown in bright-field and fluorescent images with platelets labeled with the anti-GPIX antibody (scale bars, $30 \mu\text{m}$). SPFS was performed to determine (B) adhesion forces (platelet to collagen) and (C) platelet-to-platelet interaction forces. (B and C) Representative SPFS curves from one platelet adhering to collagen or interacting with another platelet of $Myh9^{+/+}$ or $Myh9^{D1424N/+}$ sample are shown. Each data point of summary graphs (mean \pm SD) shows one platelet-to-collagen ($n = 9$) or platelet-to-platelet ($n = 7$) interaction. (D) Each data point of colloidal probe spectroscopy shows the median Young's modulus of one $Myh9^{+/+}$ or $Myh9^{D1424N/+}$ aggregate, and bar plots show means \pm SD of Young's modulus ($n = 4$). Statistics: Mann-Whitney U test (* $0.05 > P \geq 0.01$; ** $0.01 > P \geq 0.001$; and *** $P < 0.001$).

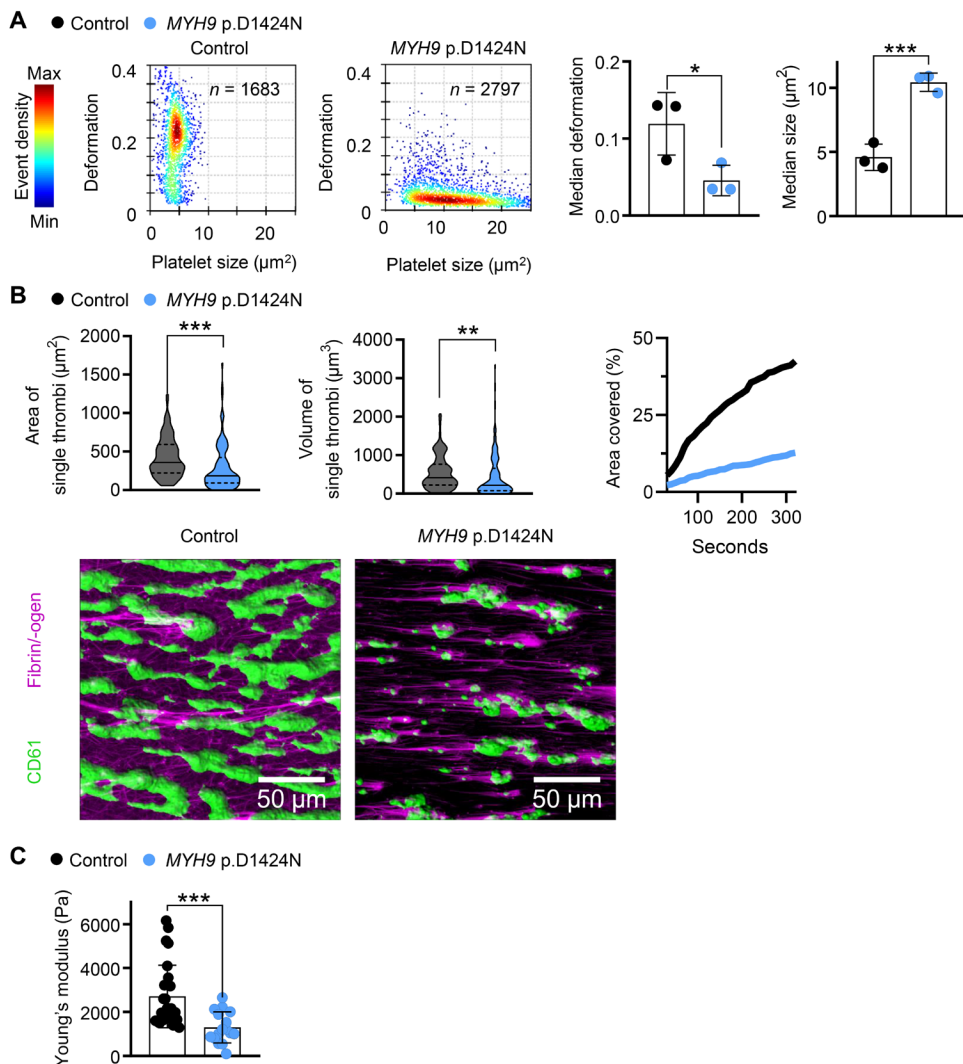


Fig. 5. Platelets of the patient with the MYH9 p.D1424N point mutation resemble the biomechanical phenotype of mouse platelets. (A) Representative kernel density estimation scatterplots from RT-FDC measurements displaying the distribution of single platelet deformation and their corresponding size between single platelets from a healthy individual (control) and from an MYH9 p.D1424N patient (n , number of single platelets). Summary data points show the median deformation or median platelet size of individual donors and one MYH9 p.D1424N patient on three different days, and bar plots show means \pm SD of deformation and size from nonstimulated platelets (multiple comparison using Holm-Sidak, $*0.05 > P \geq 0.01$ and $***P < 0.001$). (B) Platelet adhesion and aggregate formation under flow (1000 s^{-1}) on collagen of human patient samples were assessed using a flow chamber. The area and the volume of single thrombi are shown as median \pm quartiles of platelet count unadjusted conditions ($n = 100$ single thrombi). Area covered over time shows the mean of thrombi from control and patient blood. Representative images taken at the end of the perfusion time (20 min) are shown in fluorescent images with platelets labeled with the anti-CD61 antibody and labeled fibrinogen (scale bars, 50 μm). (C) Whole blood from healthy individuals and an MYH9 p.D1424N patient was examined by colloidal probe spectroscopy. Each data point shows the median Young's modulus of one healthy individual or MYH9 p.D1424N aggregate, and bar plots show means \pm SD of Young's modulus. Statistics: Mann-Whitney U test ($**0.01 > P \geq 0.001$ and $***P < 0.001$).

platelets under shear was improved in the presence of TXA (Fig. 7, B and C, and fig. S17, A and B). We measured the stiffness of the thrombi with colloidal probe spectroscopy and found that TXA significantly increased the stiffness of thrombi from the MYH9 p.D1424N sample for an extent of 1.589 (Fig. 7D). Improvement of thrombus stiffness with TXA could be achieved, however, to a lower extent by a factor of 1.20 for patient sample with E1841K mutation (fig. S17C). Together, this shows that TXA can also stabilize clots and thrombi of patients with MYH9-RD.

DISCUSSION

While the role of platelets in preventing blood loss is well characterized from a biological perspective, the mechanobiological aspects are only poorly understood. Therefore, we analyzed point-mutated *Myh9* mouse models, which recapitulate clinical manifestations observed in patients with MYH9-RD. Our study demonstrates that nonmuscle myosin IIA-mediated platelet force generation is crucial for sufficient clot compaction and hemostatic function. Our major conclusions are as follows: (i) heterozygous point mutations

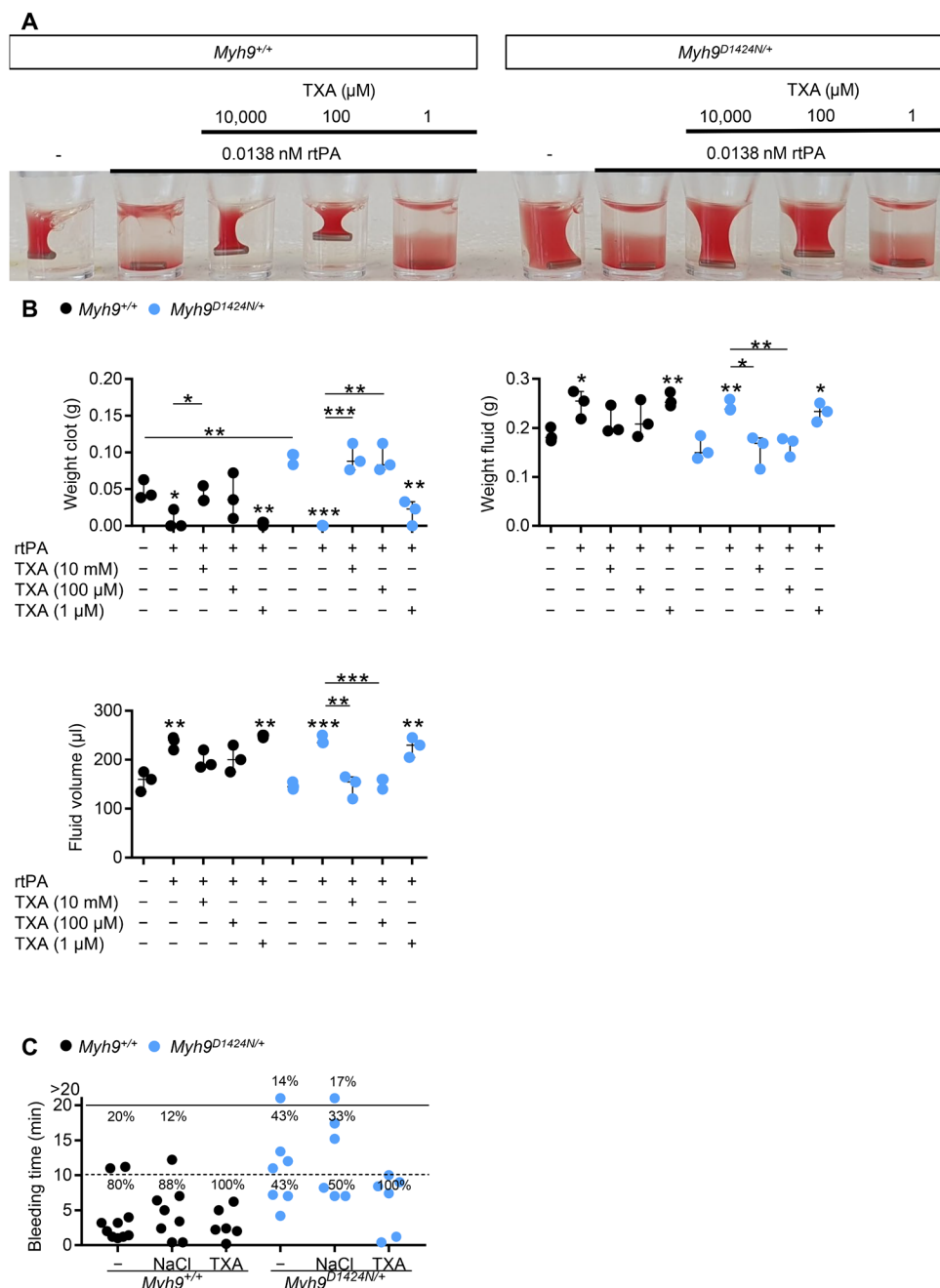


Fig. 6. Treatment with TXA improves hemostatic function in mutant mice. (A) Representative image of clot retraction from *Myh9*^{+/+} and *Myh9*^{D1424N/+} samples treated with rtPA in a threshold concentration where lysis occurs. Platelet count was not adjusted to reflect the *in vivo* situation. Addition of TXA in different concentrations 10,000, 100, and 1 μ M; representative for three independent experiments. (B) Quantification of weight clot, weight fluid, and fluid volume from clot retraction with rtPA and TXA treatment. Results are means \pm SD. Each symbol represents one individual mouse. Statistics: Mann-Whitney *U* test (ns, $P \geq 0.05$; * $0.05 > P \geq 0.01$; ** $0.01 > P \geq 0.001$; and *** $P < 0.001$). Asterisks above symbols indicate comparison to control or untreated mutant sample. (C) Tail bleeding times on filter paper of *Myh9*^{+/+} and *Myh9*^{D1424N/+} mice. Injection of sodium chloride served as injection control. Each symbol represents one individual mouse.

in the *Myh9* gene lead to reduced platelet adhesion and platelet-platelet interaction forces in mice and patients with *MYH9-RD*; (ii) impaired clot retraction and prolonged bleeding time are caused by lower platelet force generation, whereas the reduced platelet count is less critical; (iii) the mutations R702C, D1424N, and E1841K have a similar impact on the biophysical platelet function, although the

mutation E1841K had less impact on thrombus formation and stiffness; and (iv) inhibition of fibrinolysis with TXA can improve the hemostatic function in *Myh9* mutant mice.

We analyzed platelet activation of the *Myh9* R702C, D1424N, and E1841K mutant mice, which was overall comparable to controls when platelets of similar size were compared. The kinetics and

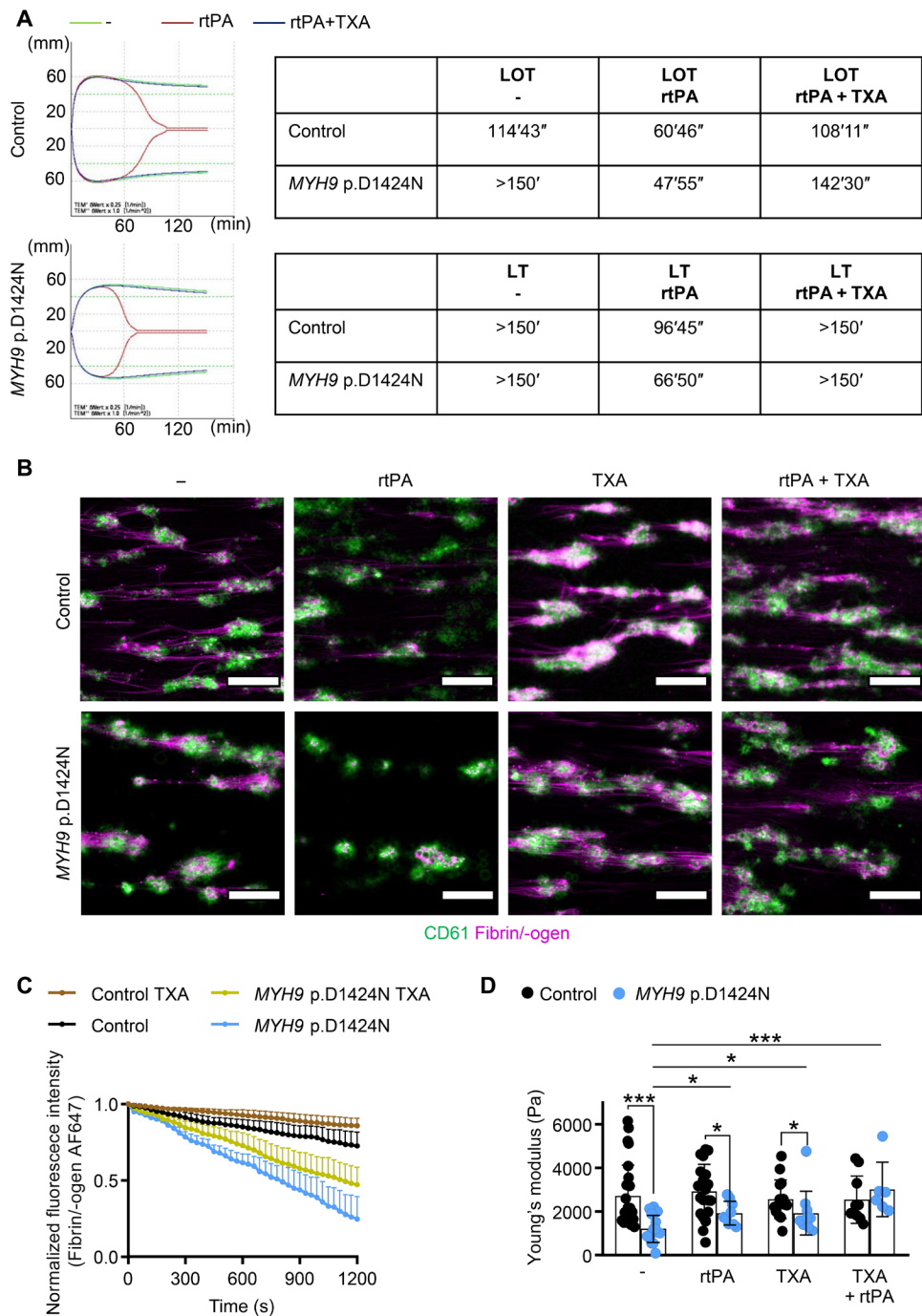


Fig. 7. TXA improves clot and thrombus stability of patient sample. (A) Lysis onset time (LOT) and lysis time (LT) assessed with rotational thromboelastometry (ROTEM) without treatment (–), stimulation with rtPA, and after the addition of TXA to contrast rtPA-induced lysis stimulation. Overlapping of the modified ROTEM analysis curves (green, no treatment; red, rtPA stimulation; blue, rtPA and TXA stimulation). (B) Representative fluorescence images of human platelet thrombi (CD61; green) and fibrin (magenta) at 20 min after treatment in a microfluidic flow chamber at a shear of 100 s^{-1} (scale bars, $50 \mu\text{m}$). (C) Time course of changes in stability of fibrinogen (normalized fluorescence of fibrinogen AF647; mean \pm SD) on sites of platelet thrombi after the addition of TXA ($100 \mu\text{M}$) compared to nontreated control. (D) Whole blood from healthy individuals and an *MYH9* p.D1424N patient was examined (untreated, with rtPA, with TXA, and with TXA + rtPA) using colloidal probe spectroscopy. Each data point shows the median Young's modulus of one healthy individual or *MYH9* p.D1424N aggregate, and bar plots show means \pm SD of Young's modulus. Statistics: Mann-Whitney *U* test (ns, $P \geq 0.05$; $*0.05 > P \geq 0.01$; and $***P < 0.001$).

extent of platelet aggregation did not differ between mutants and controls. Absent platelet shape change has been observed for myosin IIA-deficient mouse platelets (13) and patient platelets (5, 16). Unexpectedly, we observed initial platelet shape change of the mutant platelets after activation with collagen and thrombin. Myosin IIA-deficient mouse platelets have, in general, a more pronounced phenotype and thus might explain the difference (13, 17). However, the difference regarding shape change between the point-mutated mouse platelets and platelets from patients remains unclear. We detected platelet shape change in aggregometry for all three mouse lines and two different agonists, suggesting that the localization of mutation or type of agonist does not explain the difference. Thus far, the point-mutated mouse models recapitulated the key features of patients with *MYH9-RD* [(8) and our findings]. However, we cannot exclude that platelets of the patients have a more severe defect in cytoskeletal rearrangement than we observed in the mouse models.

The degree of thrombocytopenia and bleeding varies among patients with *MYH9-RD*. It was reported that the patients' platelet function is normal and severity of bleeding tendency correlates with platelet count (7, 18). It was previously demonstrated that the hemostatic function efficiently occurs at unexpectedly low platelet counts when platelets are fully functional, at least in mice (19). Therefore, our study addressed the relevance of how strongly mechanical forces contribute to the *MYH9*-related bleeding diathesis. We show that *in vitro* clot retraction of samples from *Myh9* R702C, D1424N, and E1841K point-mutated mice was impaired in both unadjusted and adjusted platelet count conditions, pointing to a less central role of the platelet count. However, clot retraction was still possible to some extent, in contrast to studies using the knockout mice with abrogated clot retraction (13). While, so far, the myosin activity inhibitor, blebbistatin, has been mainly used to analyze platelet force generation (10, 20–22), this approach cannot be used to assess the impact of the clinically relevant heterozygote mutations. Therefore, we have taken a comprehensive biophysical approach to study the mechanical properties of heterozygotously point-mutated *Myh9* platelets. Using SPFS, we demonstrate that *Myh9* R702C, D1424N, and E1841K mutant mouse platelets generate lower adhesion forces on collagen and reduced platelet-platelet interaction forces. We also measured traction forces of mutant mouse platelets on fibrinogen using a micropost deflection assay, which has already been successfully used to measure platelet contractile forces and evaluate platelet functionality (21–23). In line with the SPFS results, the average contractile force per post of mutant platelets was decreased, while the total contractile force generated per platelet of *Myh9*^{D1424N/+} mice was comparable to their corresponding controls. One possible explanation might be the enlarged size of *Myh9*^{D1424N/+} platelets combined with a higher number of surface receptors. However, for a platelet-rich thrombus, in which contractility per unit volume is the relevant parameter, forces per post must be considered. These findings support the concept (24) that the inability of platelets to generate optimal contractile forces is associated with increased bleeding and is the predominant factor over reduced platelet numbers in *MYH9-RD*. Recently, high-throughput hydrogel-based platelet-contraction cytometry, which allows quantifying single-platelet contraction forces, revealed subpopulations of highly contractile human platelets (>30 nN) and that average platelet contractile forces varied considerably among healthy donors (24). In our study, the average total contractile force generated by wild-type

mouse platelets ranged from 15.3 to 26.4 nN. However, a direct comparison of the two approaches cannot be made because of the different experimental conditions.

We further found that point-mutated *Myh9* platelets were less deformable under resting conditions (nonactivated, nonspreading platelets) as determined by high-throughput RT-FDC. However, SICM analysis unveiled that spread *Myh9*^{R702C/+} and *Myh9*^{D1424N/+} platelets are more deformable than controls. While the increased F-actin content might explain the first finding in nonactivated mutant platelets, the latter could be due to an altered actomyosin network under the platelet plasma membrane. It is tempting to speculate that the increased deformation of spread mutant platelets might contribute to the reduced traction forces. In support of this, it was shown in mouse embryonic fibroblasts that stiffer cells had a higher net contractile moment and were more prestressed than softer cells (25). Patients with *MYH9-RD* have normal red blood cell osmotic deformability as determined by ektacytometry (26). This suggests that *MYH9-RD* mutations have a distinct impact on the deformability of the two blood cell types.

We analyzed the spreading behavior of mutant mouse platelets on fibrinogen and found that heterozygous point-mutated *Myh9* mouse platelets form filopodia and lamellipodia to the same extent as controls. This is in contrast to a previous study that showed reduced lamellipodia formation and observed more unspread D1424N mutant mouse platelets (27). We even found slightly increased spreading kinetics of mutant platelets (D1424N and E1841K) at an early time point, which may probably result from the enlarged platelet size and, therefore, earlier adhesion to the activating surface. We recently showed that lamellipodial structures cannot be observed in a blood clot and therefore are dispensable for the hemostatic function and thrombus formation (28). Kim *et al.* (29) demonstrated that platelet filopodia extension and retraction are needed to transmit platelet contractile force and rearrange the fibrin matrix. In a very recent publication, the cytoskeletal structure in platelet protrusions was analyzed by applying cryo-electron tomography, revealing a nonuniform polarity of actin filaments in protrusions, indicating that this organization may allow the generation of contractile forces (30). Our data in this study demonstrate that impaired clot formation is most likely due to reduced mechanical forces and not because of a defect in shape change or cytoskeletal rearrangement. Although we did not directly analyze actin stress fiber formation upon platelet spreading, immunofluorescent and platinum replica electron microscopic images revealed that most mutant platelets were able to form stress fibers on a continuously fibrinogen-coated surface. In contrast, myosin IIA-deficient platelets are unable to form stress fiber-like structures (13). This again shows that a complete deficiency of the protein myosin IIA in platelets produces a more severe phenotype than an amino acid change on one position.

In clinics, there are different approaches to treat bleeding complications in patients with *MYH9-RD* (31). Thrombopoietin receptor agonists are an option for short-term treatment by increasing the platelet count (32). Desmopressin can be given to adults before surgery in combination with TXA. In addition, TXA is also used alone to treat excessive bleeding during menses or is locally applied after dental surgery (6, 33). Samson and colleagues showed that limited fibrinolysis paradoxically facilitates more efficient clot retraction, and TXA prevents clot shrinkage (34). However, if TXA prevents clot retraction, why is it beneficial for *MYH9*-related disease patients with bleeding complications? We hypothesized that plasminogen

could better enter the gaps between platelets and more efficiently lyse the clot because of reduced interaction forces between mutant platelets. TXA, in turn, stabilizes the clot and prevents plasmin-induced clot instability. We found that the administration of TXA could reverse the prolonged bleeding phenotype in mutant mice. Moreover, plasmin-induced clot lysis in vitro was prevented by TXA at a final concentration of 100 μ M, which is expected to inhibit fibrinolysis (15). These findings suggest that insufficient hemostatic plug compaction due to reduced forces of *Myh9* mutant platelets can be overcome by TXA-mediated clot stabilization. Concerning the increased bleeding time observed in *Myh9* mutant mice, the impact of respective point mutations on the contribution of cytoskeleton-dependent mechanical properties of the endothelial and vascular smooth muscle cells remains to be investigated. Within this context, previous work by Goeckeler *et al.* (35) in a bovine pulmonary artery endothelial cell line suggests that myosin II regulates endothelial cell tension, which is abrogated by blebbistatin, resulting in the disappearance of stress fibers. Recently, Singh *et al.* (36) demonstrated the association of nonmuscle myosin IIA with contractile filaments in mouse aortic smooth muscle cells and how it is regulated through tension-dependent phosphorylation of focal adhesion proteins.

In summary, we comprehensively analyzed the molecular and mechanical characteristics of human and mouse platelets with heterozygous point mutations in nonmuscle myosin IIA. We found that impaired clot retraction and increased bleeding tendency can be linked to reduced force generation and that interfering with the fibrinolytic system improves hemostatic function.

MATERIALS AND METHODS

Animals

Myh9 mutant mice (8) were purchased from Mutant Mouse Resource and Research Centers (MMRRC). Stock numbers are 036196-UNC (R702C), 036210-UNC (D1424N), and 036698-MU (E1841K). Wild-type littermates were used as controls for the heterozygous mice from each mutant strain because of the different backgrounds. Female and male mice were between 6 and 16 weeks of age. Animal studies were approved by the district government of Lower Franconia, Germany (license number 2-523). Mice were kept at a 12-hour light and 12-hour dark cycle with food and water available ad libitum in the experimental area of the animal facility. We followed the guidelines of ARRIVE (Animal Research: Reporting of In Vivo Experiments).

Human blood samples

The use of whole blood and platelet-rich plasma (PRP) from healthy adult individuals and patients with *MYH9*-RD was approved by the ethics committee of the University Medicine Greifswald, Germany (license number: BB 014/14). All participants gave written informed consent.

Platelet preparation

Mouse

Mice were anesthetized with isoflurane. Blood was collected in a tube containing heparin (20 U/ml; Ratiopharm), and PRP was obtained by centrifugation at 80g for 5 min at room temperature. For the preparation of washed platelets, PRP was centrifuged at 640g for 5 min at room temperature. The platelet pellet was resuspended in modified Tyrode's-Hepes buffer [134 mM NaCl, 0.34 mM Na₂HPO₄,

2.9 mM KCl, 12 mM NaHCO₃, 5 mM Hepes, 1 mM MgCl₂, 5 mM glucose, and 0.35% bovine serum albumin (BSA; pH 7.4)] in the presence of prostacyclin (0.5 μ M) and apyrase (0.02 U/ml). Platelets were lastly resuspended in the same buffer without prostacyclin (pH 7.4; apyrase, 0.02 U/ml) and incubated at 37°C for 30 min before use.

Human

The donors had not taken any medication in the previous 10 days before blood collection. Whole blood was collected by venipuncture in BD Vacutainer Tubes containing acid citrate dextrose solution A (ACD-A) and 3.8% buffered trisodium citrate (Na-citrate). Whole blood was stored at 37°C for at least 30 min. Centrifugation was not performed because the large platelets of the patients with *MYH9*-RD would sediment with the other blood cells because of their larger size. To maximize the number of platelets available for experiments (due to their reduced number in the patient sample), the ACD-A whole blood tubes were kept at a 45° angle, and PRP was transferred to a new polypropylene tube. All experimental measurements were performed within 3 hours of drawing the blood.

Immunoblotting

Washed platelets were lysed, separated by SDS-polyacrylamide gel electrophoresis, and blotted onto polyvinylidene difluoride membranes. Membranes were incubated with the respective antibodies against glyceraldehyde-3-phosphate dehydrogenase (1:1000; Sigma-Aldrich) and myosin IIA (1:200; Sigma-Aldrich). Horseradish peroxidase (HRP)-conjugated secondary antibodies and enhanced chemiluminescence solution (Bio-Rad Clarity Western ECL Substrate) were used for visualization on an Amersham Imager 680 (GE Healthcare).

Immunoblotting with ProteinSimple Jess

Protein levels of MLC2, myosin IIA, and MYPT1, and phosphorylation levels of MLC2 were analyzed using an automated capillary-based immunoassay platform (37), Jess (ProteinSimple). A total of 5×10^8 platelets/ml were lysed by the addition of equal volume ice-cold 2× lysis buffer (300 mM NaCl, 20 mM tris, 2 mM EGTA, 2 mM EDTA, 10 mM NaF, 4 mM Na₃VO₄, and 1% IGEPAL CA-630). The lysis buffer contained 2× Halt Protease and Phosphatase Inhibitor Cocktail, EDTA-Free (Thermo Scientific) to prevent protease and phosphatase activity. Lysates were diluted to the required concentration with 0.1× Sample Buffer 2 (diluted from 10× Sample Buffer 2). Lysates were prepared by the addition of 5× master mix containing 200 mM dithiothreitol and 5× sample buffer and fluorescent standards (Standard Pack 1) and boiled for 5 min at 95°C according to the manufacturer's instructions. The optimized antibody dilutions and respective lysate concentrations for each antibody (all from Cell Signaling Technology) are listed below: anti-MLC2 antibody, 1:10 and 0.1 mg/ml; anti-myosin IIA antibody, 1:10 and 0.025 mg/ml; anti-MLC2 p-S19 antibody, 1:10 and 0.4 mg/ml; and anti-MYPT1 antibody, 1:10 and 0.1 mg/ml. For most antibodies, either anti-rabbit secondary HRP antibody (DM-001) or anti-mouse secondary HRP antibody was used and the chemiluminescent signal was recorded by using the high dynamic range profile. For detection of myosin IIA, and MYPT1 signals in the R702C and E1841K knock-in samples, near-infrared (NIR) anti-rabbit secondary NIR antibody was used with the corresponding fluorescent detection profile. NIR signal is presented in grayscale. All antibodies were diluted in antibody diluent 2. Samples, antibody diluent 2, primary and secondary antibodies, luminol-S and peroxide mix, and wash buffer were displaced into 12- to 230-kDa pre-filled microplates (pre-filled with Separation

Matrix 2, Stacking Matrix 2, Split Running Buffer 2, and Matrix Removal Buffer). The microplate was centrifuged for 5 min at 2500 rpm at room temperature. To start the assays, the capillary cartridge was inserted into the cartridge holder and the microplate placed on the plate holder. To operate Jess and analyze results, Compass Software for Simple Western was used (version 4.1.0, ProteinSimple). Separation matrix loading time was set to 200 s, stacking matrix loading time was set to 15 s, sample loading time was set to 9 s, separation time was set to 30 min, separation voltage was set to 375 V, antibody diluent time was set to 5 min, primary antibody incubation time was set to 90 min, and secondary antibody incubation time was set to 30 min.

Transmission electron microscopy

Washed platelets in a concentration of 3×10^5 platelets/ μl were fixed with 2.5% glutaraldehyde (Electron Microscopy Science) in cacodylate buffer (pH 7.2, AppliChem). Epon 812 (Electron Microscopy Science) was used to embed platelets. After generation of ultrathin sections, platelets were stained with 2% uranyl acetate (Electron Microscopy Science) and lead citrate (Electron Microscopy Science). Sections were analyzed on a Zeiss EM900 electron microscope. Platinum replica electron microscopy of spread platelets was performed as previously described (28).

Flow cytometry

Whole blood was withdrawn from anesthetized mice into heparin and diluted in Tyrode's-Hepes buffer. To determine glycoprotein expression, blood was incubated for 15 min with respective fluorophore-conjugated antibodies (anti-GPIb, p0p4; anti-GPV, DOM1; anti-GPIX, p0p6; anti- α IIb β 3, JON1; anti- α 2, LEN1; anti-CD9, ULF1; anti-GPVI, JAQ1; and anti-CLEC2, INU1) (38–42). For activation studies, washed blood was resuspended in calcified Tyrode's-Hepes buffer (2 mM Ca²⁺) after washing twice with Tyrode's-Hepes buffer. Platelets were incubated with agonists for 15 min and stained with fluorophore-labeled antibodies for 15 min at room temperature. For F-actin content analysis, washed platelets were incubated with an anti-GPIX antibody derivate labeled with DyLight 649 (20 $\mu\text{g}/\text{ml}$; Emfret). Cells were fixed in 10% paraformaldehyde (PFA), centrifuged, and resuspended in Tyrode's-Hepes buffer in the presence of Ca²⁺ and 0.1% Triton X-100. Permeabilized cells were stained with 10 μM phalloidin-fluorescein isothiocyanate (FITC) for 30 min. Measurements were performed on a FACSCalibur (F-actin content of mouse line D1424N) or FACSCelesta (all others) (BioSciences, Heidelberg, Germany).

Aggregometry

Washed platelets (160 μl with 0.5×10^6 platelets/ μl) were analyzed in the presence (collagen) or absence (thrombin) of human fibrinogen (70 $\mu\text{g}/\text{ml}$; Sigma-Aldrich). Light transmission was recorded on a four-channel aggregometer (Fibrinometer, APACT, Hamburg, Germany) for 10 min and expressed in arbitrary units, with buffer representing a light transmission of 100%.

Platelet spreading

Coverslips were coated with human fibrinogen (100 $\mu\text{g}/\text{ml}$; Sigma-Aldrich) for 2 hours at 37°C. After blocking with 1% BSA in phosphate-buffered saline (PBS), coverslips were washed thrice with PBS. Platelets (3×10^5 platelets/ μl) were allowed to spread on the coated surface after the addition of thrombin (0.01 U/ml; Roche)

and Ca²⁺. After 5, 15, or 30 min, platelets were fixed with 4% PFA and permeabilized with IGEPAL CA-630. Images were taken with a Zeiss incubation microscope [$\times 100$ objective, DIC (differential interference contrast)].

Immunostaining of platelets

Fixed and permeabilized platelets were stained for myosin IIA using anti-myosin IIA (1:200 in PBS; M8064, Sigma-Aldrich) and donkey anti-rabbit immunoglobulin G–Alexa Fluor 546 antibodies (1:350 in PBS). F-actin was stained using phalloidin-Atto647N (1:500 in PBS; A22287, Invitrogen) and α -tubulin using Alexa Fluor 488-conjugated anti- α -tubulin antibodies (1:500 in PBS; sc-23948, Santa Cruz Biotechnology), respectively. Visualization was performed using a Leica TCS SP8 confocal microscope [$\times 100$ oil objective; numerical aperture (NA) 1.4]. Confocal microscopy was performed with HC PL APO CS2 objectives. Depending on the stainings, a set of monochromatic lasers (488 nm, 561 nm, and HeNe 633 nm) tuned to specific wavelengths were used. Detection filters (PMT Trans or ultrasensitive Hybrid detectors) were set to match the spectral properties of fluorochromes.

Clot retraction

PRP was filled up to a volume of 250 μl with Tyrode's-Hepes buffer to reach a platelet concentration of 3×10^5 platelets/ μl . To investigate clot retraction with unadjusted platelet count, 50 μl of PRP was filled up to 250 μl with Tyrode's-Hepes buffer and 1 μl of red blood cells. After the addition of thrombin (0.2 U/ml; Roche) and 20 mM CaCl₂, clot retraction was observed over a time period of 60 min. To investigate treatment with rtPA and TXA, concentrations of 1, 100, and 10,000 μM TXA (Merck) and 0.0138 nM rtPA (Abcam) were used and added together with thrombin and CaCl₂.

Bleeding time

Mice were anesthetized with a combination of pain reduction and narcotics (fentanyl, midazolam, and medetomidine; according to license 2-944), and a 1-mm segment of the tail tip was removed with a scalpel. Tail bleeding was monitored by gently absorbing blood with filter paper at 20-s intervals without making contact with the wound site. When no blood was observed on the paper, bleeding was determined to have ceased. Otherwise, experiments were stopped after 20 min. Bleeding times exceeding 20 min were excluded in the statistical analysis. TXA (10 $\mu\text{g}/\text{g}$; Merck) or sodium chloride, as control, was injected intravenously 5 min before cutting the tail for bleeding time experiment.

Platelet adhesion under shear flow

Mouse

Heparinized whole blood was diluted in a ratio of 2:1 in Tyrode's-Hepes buffer containing Ca²⁺ (43). Whole blood or mixed platelet count adjusted blood (5×10^5 platelets/ μl) was incubated with an anti-GPIX antibody derivate conjugated with DyLight 488 (0.2 $\mu\text{g}/\text{ml}$) at 37°C for 5 min. Coverslips were coated with Horm collagen (200 $\mu\text{g}/\text{ml}$; Nycomed) at 37°C overnight and blocked with 1% BSA in PBS for 30 min. Whole blood was perfused over coverslips in the flow chamber (slit depth, 50 μm) at shear stress equivalent to a wall shear rate of 1000 s^{-1} [Maastricht chamber (44)]. Videos and images were taken with a Leica DMI6000 B inverted microscope ($\times 63$ objective, light source Leica EL 6000, microscope controller Leica CTR6000). Analysis was performed using ImageJ software.

Human

Ex vivo thrombus formation assays were performed at a wall shear rate of 1000 s^{-1} on collagen-passivated surfaces [Horm collagen type I (200 $\mu\text{g/ml}$) from horse tendon; Nycomed] in a microfluidic parallel platelet flow chamber (on μ -Slide VI 0.1 with the following physical dimensions: width, 1 mm; height, 100 μm ; and length, 17 mm; ibidi GmbH, Germany). To visualize thrombus formation, before perfusion, platelets in ACD-A anticoagulated whole blood were stained with FITC-labeled anti-human CD61 antibody (clone: RUU-PL7F12; catalog no. 340715, BD Pharmingen, USA, used at final ratio 1:100). Fibrin formation was visualized by spiking whole blood with human fibrinogen conjugated to Alexa Fluor 647 (catalog no. F35200, Invitrogen, used at final concentration of 7.5 $\mu\text{g/ml}$). Whole blood was recalcified immediately before perfusion. Time-lapse confocal imaging (intervals of 10 s per image) was performed on a Leica SP5 confocal laser scanning microscope (Leica, Wetzlar, Germany) equipped with HCX PL APO λ blue 40.0 \times /1.25 oil objective. For image acquisition, fluorophores FITC and Alexa Fluor 647 were excited with argon-krypton (488 nm) and helium-neon (HeNe, 633 nm) laser lines, respectively, that were selected with an acousto-optic tunable filter (AOTF). Fluorescence emission was collected between 505 and 515 nm for FITC (detector HyD) and 640 to 655 nm for Alexa Fluor 647 (detector HyD). To assess the impact of TXA in some experiments, whole blood was preincubated with TXA (100 μM) for 10 min before perfusion over collagen. Impact of rtPA (137 ng/ml) on fibrin degradation was assessed under a shear flow of 100 s^{-1} , added after 10 min of thrombus formation. Quantitative assessment of platelet adhesion and thrombus formation was performed to obtain the percentage area covered by thrombi over time by computational image analysis using the surfaces creation wizard algorithm in Bitplane Imaris version 7.65 (Oxford Instruments, Abingdon, UK). Experiments were performed according to International Society on Thrombosis and Haemostasis Scientific and Standardization Committee subcommittee on Biorheology recommendations (45).

Real-time fluorescence deformability cytometry**Mouse**

Whole blood (25 μl) bled in citrate was suspended in 425 μl of Cell-Carrier B. The measurement was stopped after achieving 10,000 single platelet count (hard gate Area 0 to 40 μm^2). Using the Shape-Out analysis software (<https://github.com/ZELLMECHANIK-DRESDEN/ShapeOut2/releases/tag/2.3.0>; version 2.3; Zellmechanik Dresden, Germany), kernel density estimation plots of event density were generated, and statistical analysis using Holm-Sidak method was performed to determine the median values for platelet deformation and their size. The range area ratio was limited to 0 to 1.1, and the cell size was limited to 0 to 10 μm^2 for the analysis.

Human

Platelets in PRP were labeled with a mouse anti-human monoclonal antibody CD61-PE (phycoerythrin; catalog no. IM3605, Beckman Coulter). Incubation was performed at room temperature for 10 min in the dark. Deformation measurements were performed in a microfluidic chip with a constriction of 15 μm by 15 μm cross section and a length of 300 μm (Flic15, Zellmechanik Dresden, Germany). RT-FDC measurements were carried out in buffer CellCarrier B (Zellmechanik Dresden, Germany), which is composed of 0.6% (w/v) methylcellulose in PBS (without Ca^{2+} and Mg^{2+}). Here, 50 μl of immunofluorescently labeled human PRP was suspended in 450 μl of CellCarrier B. The human PRP suspension was then driven

through the microfluidic chip at flow rates of 0.006 $\mu\text{l/s}$, and the measurement was stopped after achieving 5000 single platelet count (hard-gate 150 to 33,000 arbitrary units for CD61-PE of fluorescence intensity) or after 10 min. RT-FDC data were acquired using the ShapeIn software (version 2.0; Zellmechanik Dresden, Germany). Using the Shape-Out analysis software, kernel density estimation plots of event density were generated, and statistical analysis was performed to determine the median values for platelet deformation and their size. The range area ratio was limited to 0 to 1.1, and the cell size was limited to 0 to 25 μm^2 for the analysis. The RT-FDC setup (AcCellerator, Zellmechanik Dresden, Germany) is built around an inverted microscope (Axio Observer A1, Carl Zeiss AG, Germany) mounted with a Zeiss A-Plan $\times 100$ NA 0.8 objective (46, 47).

Single-platelet force spectroscopy

Silicon CSC12, tipless cantilevers (0.6 N/m; MikroMasch, Tallin, Estonia), and glass-bottom 35-mm dishes (ibidi, Martinsried, Germany) were exposed to an ultraviolet (UV) cleaner (Bioforce Labs, Ames, IA, USA) for 30 min. Before coating, the cantilever spring constants were independently measured by a thermal tune procedure (JPK). Cantilevers were incubated with collagen G (50 $\mu\text{g/ml}$) for 3 hours at 37°C and rinsed three times with Tyrode's buffer. An aliquot of 15×10^3 platelets/ μl in Tyrode's buffer containing 1.0 mM CaCl_2 and 0.5 mM MgCl_2 was dropped onto the passivated glass right before each measurement (10 min, room temperature). Unbound platelets were removed by Tyrode's buffer. To immobilize a single platelet on the cantilever, the collagen-passivated cantilever was brought into contact (set point, 200 pN) with a nonactivated platelet on BSA-passivated glass slide. It was waited until a single platelet firmly adhered to the ventral surface at the tip of the cantilever. The cantilever with the adhered platelet was then moved to Horm collagen-passivated surface, and single platelets firmly attached to the Horm collagen for platelet-substrate and platelet-platelet interaction SPFS measurements, respectively. All measurements were carried out in Tyrode's with Ca^{2+} , glucose, and BSA using a JPK NanoWizard 3 (JPK, Berlin, Germany). Force-distance curves were recorded with a Z-length of 7 μm and a set point value of 200 pN to control the maximal force of the cantilever against the surface. A velocity of 15 $\mu\text{m/s}$ was used for all measurements to avoid merging of two platelets during contact and to completely rupture two platelets from each other. For each passivated substrate, the last 500 force-distance curves were taken from 7 to 10 single platelets.

Colloidal probe spectroscopy

To determine the Young's modulus of platelet aggregates, indentation experiments were performed by means of colloidal force spectroscopy using an atomic force microscope (AFM; NanoWizard 3, JPK Instruments). The AFM is combined with an optical system composed of an inverted optical microscope (IX8, Olympus; $\times 20$ objective). Gold-coated cantilevers [AFM tip: sphere (1.5 to 3 μm); catalog no. CP-qp-CONT-AU-A-5, NanoAndMore GmbH] coated with 8.45 mM poly(ethylene glycol)methyl ether thiol (Mn 800; catalog no. 729108, Sigma-Aldrich) solution for 2 hours at room temperature were used. Measurements were carried out in suspension buffer [136 mM NaCl, 0.41 mM Na_2HPO_4 , 2.65 mM KCl, 12 mM NaHCO_3 , 2.13 mM MgCl_2 , 2.0 mM CaCl_2 , 5.5 mM D-glucose, and 0.35% BSA (pH 7.4)]. Before each experiment, the sensitivity and spring constant of each cantilever were determined individually in suspension buffer. For sensitivity calibration, the cantilever deflection

upon contact with a freshly cleaved mica surface was analyzed (ensemble average, 23.3 ± 3.1 nm/V) and the spring constant was measured by thermal noise technique (ensemble average, 98 ± 30 mN/m). ACD-A human whole blood (1 ml) was treated with 7.5 μ l of 1 M $\text{CaCl}_2 \times 2 \text{ H}_2\text{O}$ and 1.88 μ l of 2 M $\text{MgCl}_2 \times 6 \text{ H}_2\text{O}$ solution. Heparinized whole blood was used for the mouse experiments. Coverslips, which were coated with Horm collagen (80 μ g/ml; Nycomed) at 37°C overnight and blocked with 1% BSA in PBS for 10 min, were installed into a flow chamber with a slit depth of 55 μ m (straight channel chip; catalog no. 20000209, microfluidic ChipShop). Recalcified whole blood was perfused at a shear stress of 1000 s^{-1} for 5 min. Coverslips were washed three times with suspension solution. The cantilever was brought into contact with platelet aggregates at a speed of 2.7 $\mu\text{m s}^{-1}$ with a force set point defined at 2 nN. Measurements were performed at room temperature in suspension buffer. Platelet Young's modulus E was calculated from AFM indentation force curves by applying the Hertz model, which describes how the force increases as the AFM probe pushes into the cell. In short, cantilever deflection force F was fitted to the equation $F(z) = \frac{4}{3} E \cdot R_{\text{sphere}}^2 \cdot z^{\frac{3}{2}} / (1 - \nu^2)$. Here, R_{sphere} is the radius of the AFM sphere probing the cells, z is the cell indentation, and the Poisson's ratio ν was set to 0.5, assuming cell volume conservation. Details can be found elsewhere (48, 49). Five platelet aggregates with at least 25 force curves per aggregate were recorded per coverslide, and each force curve was analyzed individually. Thus, for each experimental condition, platelet Young's modulus is given as the mean value of more than 100 individual force curves.

For rtPA measurements, 500 μ l of rtPA (137 ng/ml; catalog no. ab92637, Abcam) was added to the coverslide immediately after measurement of the untreated or TXA sample and incubated for 5 min. For TXA measurements, 1 ml of whole blood was incubated with 100 μ M TXA (Merck) for 10 min and further treated as described above.

Micropost assay

Micropost arrays were fabricated from hPDMS (#PP2-RG07, Gelest Inc.) by replica molding from negative molds. Micropost arrays contained cylindrical posts with a diameter of 1.05 μ m and a height of 2.6 μ m arranged on a hexagonal grid with 2.0- μ m center-to-center spacing. The Young's modulus of hPDMS was 4.7 MPa. Flat stamps for microcontact printing were made from SYLGARD 184 (Dow Corning Inc.). Fluorescently labeled (Alexa Fluor 488 NHS ester; Invitrogen) fibrinogen (Sigma-Aldrich) was physisorbed from solution (0.1 mg/ml in PBS) onto stamps for 1 hour, quickly washed with distilled water, and blow-dried under nitrogen. Coated stamps were brought into conformal contact with micropost arrays, which had been preactivated for 7 min by UV/ozone treatment, pressed down using forceps, and removed. The transfer efficiency of fibrinogen was confirmed by fluorescence microscopy of stamps and microposts and typically was >90%. Micropost arrays were passivated using a 1:2 mix (0.5 mg/ml in PBS) of fluorescently labeled (DyLight 405 NHS ester; Fisher Scientific, Ireland) endotoxin-free BSA (Sigma-Aldrich) to nonlabeled BSA for 30 min, followed by Pluronic F127 [0.5% (w/v) in PBS] for 30 min, before washing three times with PBS. Washed platelets were resuspended in Tyrode's buffer and seeded in the presence of thrombin (0.01 U/ml) onto the coverslips at a density of ~2 million cm^{-2} for 60 min at 37°C, fixed in 3% PFA in PBS for 15 min, and washed three times in PBS. Samples were permeabilized, blocked and stained for F-actin (phalloidin–Alexa Fluor 647; Invitrogen; 1:100 in 3% BSA in PBS) for 30 min, washed,

and mounted in a chamber (Chamlide; Live Cell Instruments Co. Ltd.) containing PBS. Confocal images were obtained on a Leica SP8 from top and bottom slices of the microposts. Image analysis of traction forces was performed by custom MATLAB code. Posts were detected by template matching, and their positions were refined by a radial symmetry fit. Post deflections were deduced from the positions of the same post in top and bottom slices after removal of systematic offsets between the slices. Traction forces were calculated from the post deflections by Hooke's law using a spring constant of 34.51 nN/ μ m (50).

Scanning ion conductance microscopy

Round polystyrene cell culture dishes (35 mm; Greiner Bio One, reference 627161) were coated with fibrinogen (0.1 mg/ml; Sigma-Aldrich, F3879) by incubation for 1 hour at 37°C. Washed mouse platelets were resuspended in Tyrode's buffer supplemented with 1 mM Ca^{2+} and seeded in the presence of thrombin (0.01 U/ml; Sigma-Aldrich, T6884) for 15 min at room temperature. Afterward, the culture dishes were washed three times with Tyrode's buffer to remove nonadherent platelets. The dishes were then installed in custom-built SICM setups (51) and imaged within 1 hour. Platelet morphology and elastic modulus were visualized using borosilicate pipettes with an inner radius of \approx 90 nm and an applied pressure of 10 kPa. Imaging was done at a 20-Hz pixel rate, with 32 \times 32 or 64 \times 64 pixels at scan sizes between 6 μ m by 6 μ m and 12 μ m by 12 μ m. Data were pooled from two donors. Analysis of elastic modulus E was calculated as described before (52).

Thromboelastography

Rotational thromboelastometry (ROTEM) was used with a modified version of the commercial tissue factor-activated test (EXTEM) to detect changes in fibrinolytic activity (53). In detail, we triggered the lysis ex vivo by adding rtPA (Abcam) at a final concentration of 137 ng/ml as previously reported (53). In a parallel application, we tried to contrast the lysis stimulation by contemporarily adding TXA (Merck) at a final concentration of 100 μ M, which is expected to inhibit fibrinolysis (15). The ROTEM device was from Pentapharm GmbH, Munich, Germany. The maximum runtime was set to 150 min. The following standard parameters were analyzed: LOT and lysis time in minutes.

Data analysis

Results are from at least two independent experiments per group, if not otherwise stated. Correction for multiple comparisons was analyzed using the Holm-Sidak method, and differences between control and mutant sample were statistically analyzed using the Mann-Whitney U test. P values <0.05 were considered as statistically significant: * $0.05 > P \geq 0.01$, ** $0.01 > P \geq 0.001$, and *** $P < 0.001$. Results with a P value ≥ 0.05 were considered as not significant.

SUPPLEMENTARY MATERIALS

Supplementary material for this article is available at <https://science.org/doi/10.1126/sciadv.abn2627>

[View/request a protocol for this paper from Bio-protocol.](#)

REFERENCES AND NOTES

- W. A. Lam, O. Chaudhuri, A. Crow, K. D. Webster, T.-D. Li, A. Kita, J. Huang, D. A. Fletcher, Mechanics and contraction dynamics of single platelets and implications for clot stiffening. *Nat. Mater.* **10**, 61–66 (2011).

2. Y. Qiu, J. Ciciliano, D. R. Myers, R. Tran, W. A. Lam, Platelets and physics: How platelets "feel" and respond to their mechanical microenvironment. *Blood Rev.* **29**, 377–386 (2015).
3. J. G. Drachman, Inherited thrombocytopenia: When a low platelet count does not mean ITP. *Blood* **103**, 390–398 (2004).
4. M. Seri, R. Cusano, S. Gangarossa, G. Caridi, D. Bordo, C. Lo Nigro, G. M. Ghiggeri, R. Ravazzolo, M. Savino, M. del Vecchio, M. d'Apolito, A. Iolascon, L. Z. Zelante, A. Savoia, C. L. Balduini, P. Noris, U. Magrini, S. Belletti, K. E. Heath, M. Babcock, M. J. Glucksman, E. Aliprandi, N. Bizzaro, R. J. Desnick, J. A. Martignetti, Mutations in MYH9 result in the May-Hegglin anomaly, and Fechtner and Sebastian syndromes. The May-Hegglin/Fechtner Syndrome Consortium. *Nat. Genet.* **26**, 103–105 (2000).
5. K. Althaus, A. Greinacher, MYH9-related platelet disorders. *Semin. Thromb. Hemost.* **35**, 189–203 (2009).
6. K. Althaus, J. Najm, A. Greinacher, MYH9 related platelet disorders—Often unknown and misdiagnosed. *Klin. Padiatr.* **223**, 120–125 (2011).
7. A. Pecci, C. Klfers, P. Gresele, K. J. D. Lee, D. de Rocco, V. Bozzi, G. Russo, P. G. Heller, G. Loffredo, M. Ballmaier, F. Fabris, E. Beggiato, W. H. A. Kahr, N. Pujol-Moix, H. Platokouki, C. van Geet, P. Noris, P. Yerram, C. Hermans, B. Gerber, M. Economou, M. de Groot, B. Zieger, E. de Candia, V. Fraticelli, R. Kersseboom, G. B. Piccoli, S. Zimmermann, T. Fierro, A. C. Glembotsky, F. Vianello, C. Zaninetti, E. Nicchia, C. GÜthner, C. Baronci, M. Seri, P. J. Knight, C. L. Balduini, A. Savoia, MYH9-related disease: A novel prognostic model to predict the clinical evolution of the disease based on genotype-phenotype correlations. *Hum. Mutat.* **35**, 236–247 (2014).
8. Y. Zhang, M. A. Conti, D. Malide, F. Dong, A. Wang, Y. A. Shmist, C. Liu, P. Zerfas, M. P. Daniels, C.-C. Chan, E. Kozin, B. Kachar, M. J. Kelley, J. B. Kopp, R. S. Adelstein, Mouse models of MYH9-related disease: Mutations in nonmuscle myosin II-A. *Blood* **119**, 238–250 (2012).
9. C. L. Balduini, A. Pecci, A. Savoia, Recent advances in the understanding and management of MYH9-related inherited thrombocytopenias. *Br. J. Haematol.* **154**, 161–174 (2011).
10. A. Ono, E. Westein, S. Hsiao, W. S. Nesbit, J. R. Hamilton, S. M. Schoenwaelder, S. P. Jackson, Identification of a fibrin-independent platelet contractile mechanism regulating primary hemostasis and thrombus growth. *Blood* **112**, 90–99 (2008).
11. O. Oshinowo, R. Copeland, Y. Sakurai, M. E. Fay, B. G. Petrich, T. Leong, B. Brainard, W. A. Lam, Significant differences in single-platelet biophysics exist across species but attenuate during clot formation. *Blood Adv.* **5**, 432–437 (2021).
12. J. D. Franke, A. L. Boury, N. J. Gerald, D. P. Kiehart, Native nonmuscle myosin II stability and light chain binding in *Drosophila melanogaster*. *Cell Motil. Cytoskeleton* **63**, 604–622 (2006).
13. C. Leon, A. Eckly, B. Hechler, B. Aleil, M. Freund, C. Ravanat, M. Jourdain, C. Nonne, J. Weber, R. Tiedt, M.-P. Gratacap, S. Severin, J.-P. Cazenave, F. Lanza, R. Skoda, C. Gachet, Megakaryocyte-restricted MYH9 inactivation dramatically affects hemostasis while preserving platelet aggregation and secretion. *Blood* **110**, 3183–3191 (2007).
14. D. A. Knecht, W. F. Loomis, Developmental consequences of the lack of myosin heavy chain in *Dictyostelium discoideum*. *Dev. Biol.* **128**, 178–184 (1988).
15. R. Picetti, H. Shakur-Still, R. L. Medcalf, J. F. Standing, I. Roberts, What concentration of tranexamic acid is needed to inhibit fibrinolysis? A systematic review of pharmacodynamics studies. *Blood Coagul. Fibrinolysis* **30**, 1–10 (2019).
16. I. Canobbio, P. Noris, A. Pecci, A. Balduini, C. L. Balduini, M. Torti, Altered cytoskeleton organization in platelets from patients with MYH9-related disease. *J. Thromb. Haemost.* **3**, 1026–1035 (2005).
17. F. Pertuy, A. Eckly, J. Weber, F. Proamer, J.-Y. Rinckel, F. Lanza, C. Gachet, C. Leon, Myosin IIA is critical for organelle distribution and F-actin organization in megakaryocytes and platelets. *Blood* **123**, 1261–1269 (2014).
18. A. Pecci, X. Ma, A. Savoia, R. S. Adelstein, MYH9: Structure, functions and role of non-muscle myosin IIA in human disease. *Gene* **664**, 152–167 (2018).
19. M. Morowski, T. Vögtle, P. Kraft, C. Kleinschmitz, G. Stoll, B. Nieswandt, Only severe thrombocytopenia results in bleeding and defective thrombus formation in mice. *Blood* **121**, 4938–4947 (2013).
20. L. H. Ting, S. Feghhi, N. Taparia, A. O. Smith, A. Karchin, E. Lim, A. S. John, X. Wang, T. Rue, N. J. White, N. J. Sniadecki, Contractile forces in platelet aggregates under microfluidic shear gradients reflect platelet inhibition and bleeding risk. *Nat. Commun.* **10**, 1204 (2019).
21. S. Feghhi, W. W. Tooley, N. J. Sniadecki, Nonmuscle myosin IIA regulates platelet contractile forces through rho kinase and myosin light-chain kinase. *J. Biomech. Eng.* **138**, 1045061–1045064 (2016).
22. S. Feghhi, A. D. Munday, W. W. Tooley, S. Rajsekhar, A. M. Fura, J. D. Kulman, J. A. López, N. J. Sniadecki, Glycoprotein Ib-IX-V complex transmits cytoskeletal forces that enhance platelet adhesion. *Biophys. J.* **111**, 601–608 (2016).
23. X. M. Liang, S. J. Han, J. A. Reems, D. Gao, N. J. Sniadecki, Platelet retraction force measurements using flexible post force sensors. *Lab Chip* **10**, 991–998 (2010).
24. D. R. Myers, Y. Qiu, M. E. Fay, M. Tennenbaum, D. Chester, J. Cuadrado, Y. Sakurai, J. Baek, R. Tran, J. C. Ciciliano, B. Ahn, R. G. Mannino, S. T. Bunting, C. Bennett, M. Briones, A. Fernandez-Nieves, M. L. Smith, A. C. Brown, T. Sulchek, W. A. Lam, Single-platelet nanomechanics measured by high-throughput cytometry. *Nat. Mater.* **16**, 230–235 (2017).
25. N. Schierbaum, J. Rheinlaender, T. E. Schaffer, Combined atomic force microscopy (AFM) and traction force microscopy (TFM) reveals a correlation between viscoelastic material properties and contractile prestress of living cells. *Soft Matter* **15**, 1721–1729 (2019).
26. A. S. Smith, K. Pal, R. B. Nowak, A. Demenko, C. Zaninetti, L. da Costa, R. Favier, A. Pecci, V. M. Fowler, MYH9-related disease mutations cause abnormal red blood cell morphology through increased myosin-actin binding at the membrane. *Am. J. Hematol.* **94**, 667–677 (2019).
27. K. Pal, R. Nowak, N. Billington, R. Liu, A. Ghosh, J. R. Sellers, V. M. Fowler, Megakaryocyte migration defects due to nonmuscle myosin IIA mutations underlie thrombocytopenia in MYH9-related disease. *Blood* **135**, 1887–1898 (2020).
28. Y. Schurr, A. Sperr, J. Volz, S. Beck, L. Reil, C. Kusch, P. Eiring, S. Bryson, M. Sauer, B. Nieswandt, L. Machesky, M. Bender, Platelet lamellipodium formation is not required for thrombus formation and stability. *Blood* **134**, 2318–2329 (2019).
29. O. V. Kim, R. I. Litvinov, M. S. Alber, J. W. Weisel, Quantitative structural mechanobiology of platelet-driven blood clot contraction. *Nat. Commun.* **8**, 1274 (2017).
30. S. Sorrentino, J. J. Conesa, A. Cuervo, R. Melero, B. Martins, E. Fernandez-Gimenez, F. P. de Isidro-Gomez, J. de la Morena, J.-D. Studt, C. O. S. Sorzano, M. Eibauer, J. M. Carazo, O. Medalia, Structural analysis of receptors and actin polarity in platelet protrusions. *Proc. Natl. Acad. Sci. U.S.A.* **118**, e2105004118 (2021).
31. A. Pecci, C. L. Balduini, Inherited thrombocytopenias: An updated guide for clinicians. *Blood Rev.* **48**, 100784 (2021).
32. C. Zaninetti, S. Barozzi, V. Bozzi, P. Gresele, C. L. Balduini, A. Pecci, Eltrombopag in preparation for surgery in patients with severe MYH9-related thrombocytopenia. *Am. J. Hematol.* **94**, E199–E201 (2019).
33. K. Althaus, A. Greinacher, MYH-9 related platelet disorders: Strategies for management and diagnosis. *Transfus. Med. Hemother.* **37**, 260–267 (2010).
34. A. L. Samson, I. Alwis, J. A. A. Maclean, P. Priyananda, B. Hawkett, S. M. Schoenwaelder, S. P. Jackson, Endogenous fibrinolysis facilitates clot retraction in vivo. *Blood* **130**, 2453–2462 (2017).
35. Z. M. Goekeler, P. C. Bridgman, R. B. Wysolmerski, Nonmuscle myosin II is responsible for maintaining endothelial cell basal tone and stress fiber integrity. *Am. J. Physiol. Cell Physiol.* **295**, C994–C1006 (2008).
36. K. Singh, A. B. Kim, K. G. Morgan, Non-muscle myosin II regulates aortic stiffness through effects on specific focal adhesion proteins and the non-muscle cortical cytoskeleton. *J. Cell. Mol. Med.* **25**, 2471–2483 (2021).
37. T. Heib, H. M. Hermanns, G. Manukjan, M. Englert, C. Kusch, I. C. Becker, A. Gerber, L. M. Wackerbarth, P. Burkard, T. Dandekar, J. Balkenhol, D. Jahn, S. Beck, M. Meub, S. Dütting, C. Stigloher, M. Sauer, D. Cherpokova, H. Schulze, C. Brakebusch, B. Nieswandt, Z. Nagy, I. Pleines, RhoA/Cdc42 signaling drives cytoplasmic maturation but not endomitosis in megakaryocytes. *Cell Rep.* **35**, 109102 (2021).
38. B. Nieswandt, W. Bergmeier, K. Rackebrandt, J. E. Gessner, H. Zirngibl, Identification of critical antigen-specific mechanisms in the development of immune thrombocytopenic purpura in mice. *Blood* **96**, 2520–2527 (2000).
39. B. Nieswandt, W. Bergmeier, V. Schulte, K. Rackebrandt, J. E. Gessner, H. Zirngibl, Expression and function of the mouse collagen receptor glycoprotein VI is strictly dependent on its association with the FcRγ chain. *J. Biol. Chem.* **275**, 23998–24002 (2000).
40. W. Bergmeier, K. Rackebrandt, W. Schroder, H. Zirngibl, B. Nieswandt, Structural and functional characterization of the mouse von Willebrand factor receptor GPIb-IX with novel monoclonal antibodies. *Blood* **95**, 886–893 (2000).
41. B. Nieswandt, C. Brakebusch, W. Bergmeier, V. Schulte, D. Bouvard, R. Mokhtari-Nejad, T. Lindhout, J. W. Heemskerk, H. Zirngibl, R. Fässler, Glycoprotein VI but not α2β1 integrin is essential for platelet interaction with collagen. *EMBO J.* **20**, 2120–2130 (2001).
42. F. May, I. Hagedorn, I. Pleines, M. Bender, T. Vögtle, J. Eble, M. Elvers, B. Nieswandt, CLEC-2 is an essential platelet-activating receptor in hemostasis and thrombosis. *Blood* **114**, 3464–3472 (2009).
43. Y. Schurr, M. Spindler, H. Kurz, M. Bender, The cytoskeletal crosslinking protein MACF1 is dispensable for thrombus formation and hemostasis. *Sci. Rep.* **9**, 7726 (2019).
44. L. Herfs, F. Swieringa, N. Jooss, M. Kozlowski, F. C. J. Heubel-Moenen, R. van Oerle, P. Machiels, Y. Henskens, J. W. M. Heemskerk, Multiparameter microfluidics assay of thrombus formation reveals increased sensitivity to contraction and antiplatelet agents at physiological temperature. *Thromb. Res.* **203**, 46–56 (2021).
45. P. H. Mangin, E. E. Gardiner, W. S. Nesbitt, S. W. Kerrigan, N. Korin, W. A. Lam, M. A. Panteleev; for the Subcommittee on Biorheology, In vitro flow based systems to study platelet function and thrombus formation: Recommendations for standardization: Communication from the SSC on biorheology of the ISTH. *J. Thromb. Haemost.* **18**, 748–752 (2020).
46. O. Otto, P. Rosendahl, A. Mietke, S. Golfier, C. Herold, D. Klaue, S. Girardo, S. Pagliara, A. Ekpenyong, A. Jacobi, M. Wobus, N. Töpfner, U. F. Keyser, J. Mansfeld, E. Fischer-Friedrich, J. Guck, Real-time deformability cytometry: On-the-fly cell mechanical phenotyping. *Nat. Methods* **12**, 199–202 (2015).

47. P. Rosendahl, K. Plak, A. Jacobi, M. Kraeter, N. Toepfner, O. Otto, C. Herold, M. Winzi, M. Herbig, Y. Ge, S. Girardo, K. Wagner, B. Baum, J. Guck, Real-time fluorescence and deformability cytometry. *Nat. Methods* **15**, 355–358 (2018).
48. A. Weber, J. Iturri, R. Benitez, J. L. Toca-Herrera, Measuring biomaterials mechanics with atomic force microscopy. 1. Influence of the loading rate and applied force (pyramidal tips). *Microsc. Res. Tech.* **82**, 1392–1400 (2019).
49. M. Glaubitz, N. Medvedev, D. Pussak, L. Hartmann, S. Schmidt, C. A. Helm, M. Delcea, A novel contact model for AFM indentation experiments on soft spherical cell-like particles. *Soft Matter* **10**, 6732–6741 (2014).
50. I. Schoen, W. Hu, E. Klotzsch, V. Vogel, Probing cellular traction forces by micropillar arrays: Contribution of substrate warping to pillar deflection. *Nano Lett.* **10**, 1823–1830 (2010).
51. J. Seifert, J. Rheinlaender, F. Lang, M. Gawaz, T. E. Schaffer, Thrombin-induced cytoskeleton dynamics in spread human platelets observed with fast scanning ion conductance microscopy. *Sci. Rep.* **7**, 4810 (2017).
52. J. Rheinlaender, S. Vogel, J. Seifert, M. Schächtele, O. Borst, F. Lang, M. Gawaz, T. E. Schäffer, Imaging the elastic modulus of human platelets during thrombin-induced activation using scanning ion conductance microscopy. *Thromb. Haemost.* **113**, 305–311 (2015).
53. G. J. A. J. M. Kuiper, M.-C. F. Kleinegris, R. van Oerle, H. M. H. Spronk, M. D. Lancé, H. T. Cate, Y. M. C. Henskens, Validation of a modified thromboelastometry approach to detect changes in fibrinolytic activity. *Thromb. J.* **14**, 1 (2016).

Acknowledgments: We thank D. Naumann, K. Ulbrich, T. Nahm, D. Biedenweg, M. Emanuel, N. Thi-Huong, J. Klauke, R. Raschke, and J. Wesche for excellent technical assistance. **Funding:** This work was supported by TR240 grant with project number 374031971 of the Deutsche Forschungsgemeinschaft (DFG; German Research Foundation), by the Deutsches Zentrum für Herz-Kreislauf-Forschung (Postdoc Start-up Grant under grant agreement 81X3400107), by the Bundesministerium für Bildung und Forschung (ZIK grant under grant agreement 03Z22CN11), and by the DFG project number 335549539/GRK2381. I.S. acknowledges funding from RCSI. **Author contributions:** Performed experiments: J.B., L.S., O.O., I.S., C.Z., R.K., H.v.E., J.R., Z.N., R.P., and M.B. Data analysis: all authors. Writing—original draft: J.B., L.S., R.P., and M.B. Supervised research: O.O., A.G., T.E.S., R.P., and M.B. Funding acquisition: O.O., I.S., T.E.S., R.P., and M.B. All authors have critically revised and approved the final version of the manuscript. **Competing interests:** O.O. is co-founder and shareholder of Zellmechanik Dresden distributing the Accellerator for real-time fluorescence and deformability cytometry measurements. The authors declare no other competing interests. **Data and materials availability:** All data needed to evaluate the conclusions in the paper are present in the paper and/or the Supplementary Materials.

Submitted 15 November 2021

Accepted 1 April 2022

Published 18 May 2022

10.1126/sciadv.abn2627